University of London
Imperial College of Science, Technology and Medicine
Department of Physics

Entanglement Entropy Spectrum for Bosonic Circuit with Tensor Network State

Auther: Man Hei Cheng
Supervisor: Prof. Myungshik Kim

Submitted in part fulfilment of the requirements for the degree of
Master of Science of Imperial College London and
the Diploma of Imperial College, September 2021

Abstract

This dissertation consists of two parts. First, we review the formalism of the tensor network state (TNS). We briefly introduce the types of TNS, explain the one-dimensional matrix product state (MPS) in detail, and explore the charge conservation law for TNS. In the second part, we study different types of bosonic quantum circuits, and the scaling of entanglement entropy analytic upper bound, to decide what circuit type is classically hard to simulate. In particular, we focus on the circuit of multiple quantum optical fibre loops set-up, and boson sampling device, where the analytic upper bounds of the entropy are derived theoretically and numerically. The results of the derivation are compared to the simulation made by MPS. It is possible to decide the hardness of simulation with entanglement entropy because it directly measures the complexity of quantum many bodies problem. The technique of this analysis is therefore useful for gauging quantum supremacy, important for the NISQ era[1][2].

Acknowledgements

I would like to express my gratitude to:

- Prof. M. Kim for this amazing opportunity and his continuous support that allows me to explore the topic of bosonic circuits with great autonomy.
- Dr. Antonio A. Valido for his recommendations of my reading lists and discussions
- Prof. K. Stelle for his encouragement while I was facing difficulty in the simulation.
- My parents' continuous financial support despite of the expensive international fee and circumstances.
- H. Abdurehim for being my friend while both of us were going through tremedous difficulties in our lives.

Dedication

Dedicated to the truth.

‘What you seek is seeking you.’

–Rumi

Contents

Abstract i

Acknowledgements iii

1 Introduction 1

1.1 Motivation and Objectives 1

1.2 Statement of Originality 3

2 Tensor Network Overview 4

2.1 Tensor Network Starter Pack 4

2.2 Tensor Network as Quantum State 7

2.3 Types of TNS 7

2.4 Schmidt Decomposition 9

3 The Matrix Product States 11

3.1 Definition and Basic Properties 11

3.1.1 Power of the Canonical Form 12

3.1.2 Limit of Canonical Form 17

3.2 Time Evolving Block Desimation (TEBD) 18

4 Conservation Law of TNS 23

4.1 Abelian Charge Conservation 23

4.1.1 Examples 23

4.1.2 Abelian Charge Selection Rule 26

4.2 Abelian Charge Summation Rule in TNS 27

4.3 Non-Abelian Charge Conservation 28

4.3.1 Property of Operator with Charge q_1 29

4.3.2 Non-Abelian Charge Structure of a TNS 30

5 Bosonic Quantum Circuit 34

5.1 Motivation 34

5.2 Tensor Representation of Beam-Splitter 35

5.3 Entanglement Entropy by a Single Beam Splitter 36

5.4 Photonic Quantum Information Encoding 37

5.4.1 Single and Multiple Fibre Loops 38

5.4.2 Boson Sampling Bosonic Circuit 44

5.4.3 Entanglement Spectrum for Low Transmission Coefficient with non-linear Interaction Term 46

6 Simulation Results 51

6.1 Single Fibre Loops 51

6.1.1 Simulation Method 51

6.1.2 Sanity Check 51

6.1.3 Entanglement Entropy 53

6.1.4 Implication of the Area Law for Simulation 54

6.2 Two Fibre Loops 55

6.2.1 Loops in Sequence 55

6.2.2 Two Sequential Loops Entanglement Entropy 56

6.2.3 Non-sequential Two Fibre Loop 57

6.2.4 Loop in Loop Entanglement Entropy 57

6.2.5 Discussion – Complexity for Fibre Loops 58

6.3 Boson Sampling 61

6.3.1 Simulation Method 61

6.3.2 Sanity Check 61

6.3.3 Low Transmission Coefficient with Cross Kerr Interaction 62

6.3.4 Free Bosons 62

6.3.5 Classical Simulatability of Boson Sampling Device 63

6.3.6 Discussion of Boson Sampling Entanglement Entropy 65

6.4 General Discussion 68

7 Conclusion 70

7.1 Summary of Thesis Achievements 70

7.2 Applications 71

7.3 Future Work 72

A Appendix 73

A.1 Existence of the Canonical Form 73

A.2 TEBD Preserves Canonical Form 75

A.3 Two fibre loops Canonical Form 76

Bibliography **76**

List of Tables

6.1 It is not clear in this plot whether the maximal entropy is bounded from above, so a table is made to compare the bound and the entropy for $\langle n \rangle = 1, 2, 3, 4$. . . 53

List of Figures

2.1 A rank (m, n) tensor is depicted as a node with n edges as the bra indices pointing in and m edges as the ket indices pointing out. Direction of the arrow indices whether the index tranform covariantly or contravariantly. For example, a scalar is a node without edges, a vector is a node with one edge, and so on. 5

2.2 Given two tensors A and B, tensor contraction of one pair of indices β - β is represented as bond between the tensors while keeping other indices like α and γ untouched. noticed that the bond is not assigned with a direction because the direction does not affect the contraction. Meanwhile, the uncontracted edges are a collections of bra and ket indices, so no direction is assigned either. 5

2.3 a) inner product between vectors A and B; b) matrix transformation A on vector B; c) matrix product; d) trace of matrix product $ABCD$. 6

2.4 The diagram is a fragment of 2D 1-site unit cell Z PEPS, where the boundary is not specified and can be open, close, or periodic. In general, PEPS can admit other lattice structures such as the honeycomb shape and is not limited to one type of unit cell. The uncontracted edges are assigned with an out-pointing arrow to denote the ket indices. 8

2.5 [3] The diagram is the illustration of the 1D MERA with a 2D holographic geometry. Beside the spatial dimension x, MERA has an extra length scale dimension z that measures the exponentially growing system size. In this example, the edge state serves as a hologram of the geometry of the total TN. The state is two dimensional because the number of open indices are proportional to the lattice area. The isometric tensor is the three legs tensor and disentangler is the four legs tensor in this diagram. 9

3.1 a) open boundary MPS; b) periodic boundary MPS. We can see that the uncontracted edge numbers is proportional to the length of the array in this case. . . . 11

3.2 a) represents the isometric property of $Q^{\sigma_1}_{b_1}$ in its canonical form. Straight line on the RHS represents $\delta_{m,n}$ b) represents the isometric property of $Q^{\sigma_i}_{b_{i-1},b_i}$. Combining properties a) and b), we can show in c) that the left canonical form must be an orthonormal basis. We can perform the same calculation for the right canonical form to find that they also represent the orthonormal basis. Note that Q^* represent the Hermitean conjugate of Q here. 14

3.3 In the canonical form, the Schmidt basis cancels itself. Calculation of the expectation $\langle\mathcal{O}\rangle$ requires only the contraction of the local indices. Since the canonical form does not alter the physical legs, there is no need to transform the operator basis state for the contraction. 17

3.4 A brief argument why the canonical decomposition is useful in giving the upper bound of the entanglement entropy. a) Consider a direct product system $A \cup A^c \otimes B \cup B^c$. Applying cuts to $A \cup A^c$ and $B \cup B^c$ in the middle simultaneously gives the product density matrix $\rho_{AB} = \rho_A \rho_B$, and thus the corresponding entanglement entropy $S(\rho_A) + S(\rho_B)$. b) Now we introduce entanglement between $A \cup A^c$ and $B \cup B^c$, then the mutual information, defined as the LHS of the first line, is > 0, so the entanglement entropy is smaller than the sum of the entanglement entropy of ρ_A and ρ_B. Back to periodic MPS, the singular values are precisely where the cuts located. 18

3.5 a) contract site tensors that are involved in a local time evolution together. b) time evolution. c) SVD to obtain the new singular values and site tensors. Bonds within the retangular box are contracted and otherwise left untouched. 22

4.1 a) is the TN representation of CGC. The intersection is where the tensor locates. b), c) are the orthonormal conditions of CGC, where the straight line(s) denotes the Kronecker deltas. The pair (q, q_z) is compactly written as i. The connected edge is a tensor contraction between two CGCs. In finite-dimensional Hilbert space, either b) or c) must be a projection operator, but not applicable here. . . 31

4.2 This is the generalisation of Wigner-Eckart theorem to tensor with 4 legs. The (i, j, k, l) indices denotes the pair (qq_z), while p is just the charge label. It can be shown that the tensor can be decomposed into the reduced matrix element with 5 legs and a CGC network. Such decomposition remains valid for tensors with n legs. 32

5.1 a) Experimental set-up of the single fibre loop, where N time-bin modes $\mathcal{T}_i$ are sent regularly to the loop $\mathcal{L}$, resulting in mixing via the unitary operator U among the modes and complexity in the N output modes $\tilde{\mathcal{T}}_i$; b) Quantum circuit representation of the set-up, where the fibre loop is represented as a ladder of unitary operations between every adjacent time-bin modes. 38

5.2 This is the MPS representation of the single fibre loop. This representation is equivalent to b) in fig. 5.1 in the sense that the operation order of U and thus the relative entanglement structure is not changed by deforming b) to the MPS representation here. This is indeed the power of categorical quantum mechanics.[4] 39

5.3 This is the TN representation of unitarity of the beam splitter operator. The unitary operator has outgoing arrows whilst its inverse has incoming arrows. Diagrammatically, it is a statement on the topological property of the four legs unitary operators, that is, the equivalence of intersecting and non intersecting lines. The resulting non-intersected lines represent the two Kronecker deltas. . . 39

5.4 To calculate the normalisation with tensor network, we just need to iteratively unintersects the time-bin lines, $|n_1\rangle, |n_2\rangle, ..., |n_N\rangle$ and the loop line $|0\rangle$. The third equality is trivially obtained because $\langle n|n\rangle$=1 39

5.5 Contraction the right side of the MPS immediately gives the Kronecker delta, meaning that the future operation, the future output time bin mode relative to the ith bipartition is already in a canonical form. 40

5.6 This diagram is the generalised representation of fibre loops set-up in a multi-fibre loops scenarios. The time-bin modes vector T_i represents a collection of initial time-bin modes, and $\mathcal{L}_i$ similarly represents a collection of loop states. The unitary operator here is understood as a collection of local beam-splitter operators. Indeed, a collection of unitary operators is still unitary. Thus, in the generalised set-up, so the identity property of the unitary operator is still satisfied. However, identity is now over the composite initial loop state basis. . . 41

5.7 Putting the generalised MPS into the canonical form, and the right side never contributes to the QR decomposition. 41

5.8 The diagram on the left represents the density matrix of an subsystem size $L = 6$ (characterised by its 6 outputs) of the boson sampling tensor network of size $L = 12$. The top triangles are the 12 initial input states, and we trace over the left subsystem to obtain the density matrix. In the middle, we perform operation in eqn. 5.23 to eliminate the unitary evolution that contributes only to the right subsystem. Finally, we isolate the part of the TN that contributes to the bipartite entanglement entropy. 45

6.1 This diagram shows the expected photon number of the output time-bin mode in log-log scale. We can see that the initial photon number matches τ, and the final output photon number reaches the universal equilibrium – $\langle n\rangle = 1$ 52

6.2 This diagram shows the expected photon numbers of the loop mode in log-log scale. We see that the initial loop mode photon is instead proportional to the reflection coefficient. Thus, the conservation of photon number is satisfied. Meanwhile, the final loop photon number too reaches the universal equilibrium – $\langle n \rangle = 1$. 52

6.3 This diagram shows the loop entanglement entropy between the loop state and the past output time-bin mode. All entanglement entropies saturate at a maximum value for all tested transmission coefficients, demonstrating the area law of single fibre loop. 53

6.4 This diagram shows the analytic upper bound and the maximal entanglement entropy concerning the average photon number in the loop mode. We see that the bound is tight, meaning that the prediction is correct. This plot also informs us that the entanglement entropy scales logarithmically with the number of input photon. A slight deviation appears between the bound and the max entropy at high $\langle n_L \rangle$ because the bond dimension is fixed at $nl = 30$ for increasing expected loop photon number in this plot. 54

6.5 This diagram shows the optical set-up of two fibre loops in sequence. The TN representation is available in the appendix. 55

6.6 This diagram shows the optical set-up of two fibre loops with one within the other. The TN representation is available in the appendix. 55

6.7 This diagram shows the photon number of the second loop state. We see that there is two equilibrium in the second loop state. The first equilibrium appears when the second loop state saturates before the first loop does. When the first loop is saturated, however, more photons are available for the second loop state such that the second loop state rises to its final equilibrium. 56

6.8 This diagram shows the two sequential loops entanglement entropy time evolution. Again, all entanglement entropy saturate despite of the transmission coefficient. 56

6.9 This diagram shows the analytic upper bound vs. max numerical entanglement entropy for two loops in series. It is much clearer this time that the numerical upper bound is systematically lower than the analytical upper bound for all photon numbers. Again the deviation for large photon number at the RHS of the plot is due to a non-sufficiently large enough bond dimension. 57

6.10 This diagram shows the expected photon number of the first loop state. Except for the case of low transmission coefficient, the photon number in the first loop increases in an interesting zigzag manner. That is because the photon number appears to oscillate between the first and the second loop. 58

6.11 This diagram shows the expected photon number of the second loop state. Notice that the oscillation that is complementary to the first loop state. 59

6.12 This diagram shows the loop in loop entanglement entropy time evolution. All entropy saturate as before despite the transmission coefficient. What is perhaps more unique is the transient state. At $\tau = 0.1$, it takes a much longer time $\sim 10^2$ for the loop and loop set-up up to saturate compared to the loops in sequence $\sim 4 \times 10^0$. This suggests that the loop in loop set-up produces more complex dynamics in the loop states. 60

6.13 This diagram shows the analytic Upper bound vs. max numerical entanglement entropy for the loop in loop set-up. Compared to the two loops in sequence, the analytic upper bound is rather tight compared to the numerical result, and this again suggests more complex dynamics in the loop in loop set-up. 60

6.14 Entanglement entropy of non-linear sampling device vs. the analytic upper bound. The sampling device is run over 50 layers with system size $L = 10$ such that the system reaches an equilibrium. The result confirms that the upper bound is indeed the right description for non-linear sampling devices. Entanglement entropy of this type is an example of Page curve, funny enough[5]. 63

6.15 Without the interaction term, photons within the sampling device interact linearly as superposition, so thermalisation does not take place. Instead, we need another description of the entanglement entropy. 64

6.16 This diagram shows the Hilbert space distribution across the boson sampling device. The numerical result shows that the distribution is parabolic in the log plot. 65

6.17 This diagram shows the singular value of an example bipartition at $L = 5$. The distribution is almost flat, meaning that the system resembles a random pure state rather than a thermal state. Computationally speaking, a truncation to the bond dimension (that holds the singular value) in this case would be harmful to the simulation. 66

6.18 Despite of the transmission coefficient τ, the entanglement entropy spectrum of the boson sampling device in equilibrium remains the same. It implies that one only needs to derive one universal upper bound to characterise the boson sampling entanglement entropy spectrum. 67

6.19 The estimate upper bound for system size $L = 10$ is compared to the analytic upper bound to Page's upper bound given by eqn. 5.25, upper bound based on the Hilbert space dimension in the virtual legs, and the numerical entropy in equilibrium. First, we observe that Page's upper bound deviates from the numerical result because of the finite size of boson sampling device; the Hilbert space dimension estimation is to further justify that the singular value distribution are flat for all subsystem size; otherwise, the calculation will deviate a lot from the numerical result. Finally, we can see that our estimated upper bound does describe the entanglement entropy with small systematic deviation. 67

A.1 First, we Schmidt decompose the first bond using the QR and LQ decomposition as shown in fig. A.1. Comparing (1) to the full canonical form we find out the form of the boundary Γ_1 tensor, which satisfies eqn. 3.5, because $U_1^\dagger$ is unitary. . 73

A.2 You need better explanation here. We proceed to Schmidt decompose the second bond. 74

A.3 Comparing (2) with the canonical form, we obtain form of the bulk Γ_2 tensor. We can explicitly check that $S_1\Gamma_2$ satisfies eqn. 3.13. 74

A.4 Meanwhile, we demand that $\Gamma_2 S_2$ needs to satisfy eqn. 3.14. Comparing (1) and (2), we can simply the equation $\Gamma_2 S_2 = S_1^{-1} U_1 Q_2 M_2^{\dagger} S_2$. 74

A.5 Thus, we also verify eqn. 3.14. The rest of the tensor Γ_i can be constructed via the same method, and they must all satisfy (3) and (4) by construction. 74

A.6 Consider two lattice sites A and B of the canonical form with three singular values s_1, s_2 and s_3. We operate U obtained from Suzuki-Trotter decomposition on the physical legs and SVD to obtain the new "canonical form". By definition of SVD, $s_2 A'$ and $B' s_3$ are guaranteed to be isometric, but we want to show that $A' s_2'$ and $s_2' B'$ are also isometric. 75

A.7 By unitarity, we observe that $s_1 A' s_2' B'$ must be isometric simply because $s_1 A s_2 B$ is isometric. 75

A.8 Meanwhile, as mentioned in the beginning, $s_1 A'$ is also isometric due to property of SVD, so $s_2' B'$ is also isometric. With the same reasoning, it is also true for $A' s_2'$. Thus, the new MPS is in canonical form! 75

A.9 TNS representations of two loops architecture: the top TNS represents the TNS for the loops in sequence architecture, and the bottom one represents the TNS for the loop in loop architecture. The intersection is where the unitary operator locates and the time direction specifies by the arrow, is how to identify the unitarity. 76

A.10 By the property of unitarity, the right side of the MPS can be reduced to the Kronecker delta simply due to unitarity, and that implies that the right side of the two loops architecture is always isometric, thus does not contribute to the entanglement. 77

Chapter 1

Introduction

1.1 Motivation and Objectives

To summarise tensor network state (TNS) in a sentence: it is a network of entanglements. Theoretically, it describes quantum mechanics categorically; computationally, it introduces a data structure that simulates a class of useful quantum systems; TNS as an entanglement network allows it to classify the hardness of simulation with classical computer.

Due to the fundamental role of entanglement in physics, TNS finds its application across disciplines of physics and beyond. In mathematical physics, TNS can be defined as the Penrose notation[6][7]; in category theory, it is called the string diagram[8]; in quantum information, it is called the ZX calculus[9]; fun fact, TN theory also finds application in modeling brain function in neuroscience[10]. Finally, it is the condensed matter physicists who named coined the name TNS[11].

Generally speaking, when studying a quantum many-body problem, there are two main objectives: constructing the quantum state (whether as an approximation or exact) and determining the physical quantities. In TNS, singular value decomposition (SVD) or the QR decomposition can be used to calculate the entropy[12], and tensor contraction to calculate the desired correlation function. These are simple to learn yet efficient methods to simulate quantum phenomenon[11].

The key feature that makes TNS useful in achieving both objectives is that it exploits network decomposition to simplify the problem of interest from an exponentially hard to a polynomial-time problem. Indeed, one can understand the geometry of a TNS as the geometry of entanglement[3], and understanding this entanglement structure is the key to simplification.

In the dissertation, we focus on a one-dimensional example of TNS – the matrix product state(MPS). In MPS, the geometry is manifested as a one-dimensional chain of uncontracted tensors. The chain can be further simplified to the canonical form. It is fundamental to methods like Time Evolved Blocked Decimation (TEBD)[13] for time evolution and Density Matrix Renormalisation Group (DMRG)[14] for ground state approximation.

However, TNS is not without its limitations. For example, it can be shown that any one-dimensional quantum system can be decomposed into a MPS, but not all one-dimensional systems are entangled only to their local neighbors. Whether the MPS can be efficiently simulated then relies on how the entanglement entropy between two subsystems scales when the boundary that splits the system changes. If the entanglement entropy scales with the subsystem size, then the interaction is non-local and we will need a quantum computer to perform the simulation. Otherwise, if the entanglement entropy scales with the boundary size, interaction is local and viola a classical computer can handle this problem![15] It is a common practice to benchmark what system is classically simulable by checking the scaling of the entanglement.

Theoretically speaking, not only is the TNS a framework of quantum many-body problems, but also a framework that captures the relationship between entanglement and geometry, and potentially the language to understand quantum gravity. It has been shown that the TNS can reconstruct the discretised version of AdS/CFT correspondence[16]. Not to mention that it is a natural language for simulating other quantum gravity frameworks such as the spin network (LQG)[17]. There has been an effort to seek the connection between LQG and string theory via the TNS[18].

Although TNS theory has thus far been a huge success in condensed matter theory, its full power has yet to be fully explored. Therefore, it motivates this dissertation to explore the use of TNS in quantum optics where we classify the types of bosonic quantum circuits. Meanwhile, this dissertation tries to provide enough information for readers to construct their own TNS from scratch. We hope that by the end of the dissertation readers can appreciate that the formalism of TN is both useful for simulation and theoretical analysis.

The first part of this dissertation serves as a review of TNS. We introduce the matrix product state (MPS) and study its two key properties - canonical forms and charge information - in great detail. In particular, proofs of the properties that are unavailable in the literature are included. Extra attention are paid to the non-Abelian charge conservation of the TNS because of its beautiful properties and importance.

In the second part, we investigate how to convert a beam splitter to a matrix product operator (MPO) from the Fock-space description, and study the entanglement entropy of input photons that interact in the architecture of beam-splitters. Two types of bosonic circuits are investigated – fibre loops and boson sampling – that respectively correspond to sequential and parallel operations of the beam splitters. We theoretically derive the entanglement entropy analytical upper bounds of both the fibre loops and boson sampling architectures, then the bounds are examined by simulations with TNS.

1.2 Statement of Originality

This is to certify that to the best of my knowledge, the content of this thesis is my own work. This thesis has not been submitted for any degree or other purposes.

Chapter 2

Tensor Network Overview

As mentioned in the introduction, TNS plays an important role in the simulation of quantum many body problems. Due to its categorical nature, it finds applications across fields of physics and beyond. Understanding TNS is not only helpful for gaining new computational skill, but also essential in gaining new insights into the nature of quantum physics.

2.1 Tensor Network Starter Pack

This section briefly introduces graphical representation tensor in the TNS and the construction of TNS from tensors. Then, we quickly skim through the types of TN structures and provide references on them for curious readers. For the sake of completeness, we will define a tensor here. A rank-(m, n) tensor with the n-basis and the m-dual basis transforms like:

$$\hat{T}^{k_1...k_m}_{i_1...i_n} \to \hat{T}'^{k_1...k_m}_{i_1...i_n} = M_{i_1}^{j_1}...M_{i_n}^{j_1}(M^{-1})^{k_1}_{l_1}...(M^{-1})^{k_m}_{l_m}\hat{T}^{l_1...l_m}_{j_1...j_n} \tag{2.1}$$

where the m indices transform contravariantly by the group representation M, and the n indices transform covariantly by the dual representation M^{-1}. In TN, a single tensor $\hat{T}^{k_1...k_m}_{i_1...i_n}$ is modelled as a node with $n+m$ edges, see fig. 2.1.

Meanwhile, tensor contraction is a generalisation of inner product and matrix product. One

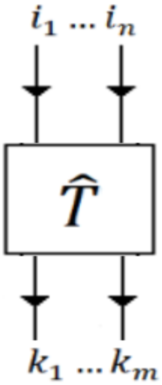

Figure 2.1: A rank (m, n) tensor is depicted as a node with n edges as the bra indices pointing in and m edges as the ket indices pointing out. Direction of the arrow indices whether the index tranform covariantly or contravariantly. For example, a scalar is a node without edges, a vector is a node with one edge, and so on.

index contraction is mathematically written as:

$$C_{\alpha\dots\gamma} = A^{\beta}_{\alpha\dots} B_{\beta\dots\gamma} \tag{2.2}$$

where the Einstein summation convention is used here. Such contraction connects one edge of A with B as shown in fig. 2.2.

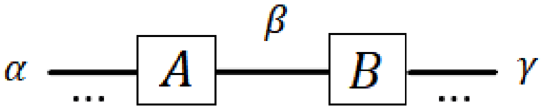

Figure 2.2: Given two tensors A and B, tensor contraction of one pair of indices β - β is represented as bond between the tensors while keeping other indices like α and γ untouched. noticed that the bond is not assigned with a direction because the direction does not affect the contraction. Meanwhile, the uncontracted edges are a collections of bra and ket indices, so no direction is assigned either.

To generalise, n connected edges between A and B represents n pairs of indices contraction, so tensor product $A \otimes B$ is pair of unconnected nodes[1]. More examples of tensor contractions can be found in fig. 2.3. TN is an elegant structure consisted of individual tensors and connections between them. In particular, the network allows us to inspect the most efficient order to

---

[1] we can also represent it as a connected node with one entry in the index β

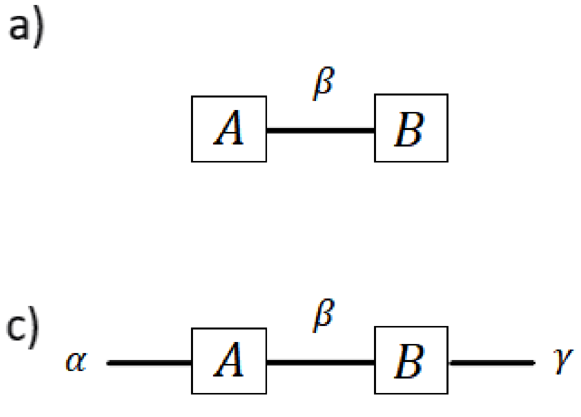
a)
β
A
B
b)
α
β
A
B
c)
α
β
γ
A
B
d)
β
A
B
α
γ
D
C
λ

Figure 2.3: a) inner product between vectors A and B; b) matrix transformation A on vector B; c) matrix product; d) trace of matrix product $ABCD$.

contraction of all of the indices when dealing with complex arithmetic[11].

2.2 Tensor Network as Quantum State

A general d-level n-particle wave function $|\Phi\rangle$ can be written as:

$$|\Phi\rangle = \sum_{i_1 ... i_n} C^{i_1 ... i_n} |i_1\rangle \otimes ... \otimes |i_n\rangle \tag{2.3}$$

where i_m ranges from 1 to d. A many body state-vector is basically a tensor with indices running over the quantum numbers of the wave function.

Such tensor can maximally contain d^n coefficients, thus exponentially difficult to store as we increase the system size. Instead of storing a massive rank n tensor, TN decomposes the tensor into a network of smaller constituent tensors, and stores the constituent tensors individually and the network of contraction. On physical ground, such decomposition is possible because the collective properties of a many-body quantum system, described by that rank n tensor, emerge from simpler properties of the building blocks. Examples of the decomposition can be found in the chapter 3.

2.3 Types of TNS

There are three main structures to TN:

- Matrix Product States(MPS)
- Projected Entanglement Pairs States(PEPS)[19]
- Multi-Scale Entanglement Renormalisation Ansatz(MERA)[20]

MPS formalism is a method to simulate 1D quantum many-body system. Its properties are covered in the MPS section.

PEPS is a 2-dimensional analogue of the 1D MPS lattice useful for simulating two-dimensional system, see fig. 2.4 for more information. The constituent sites only need to obey the normali-

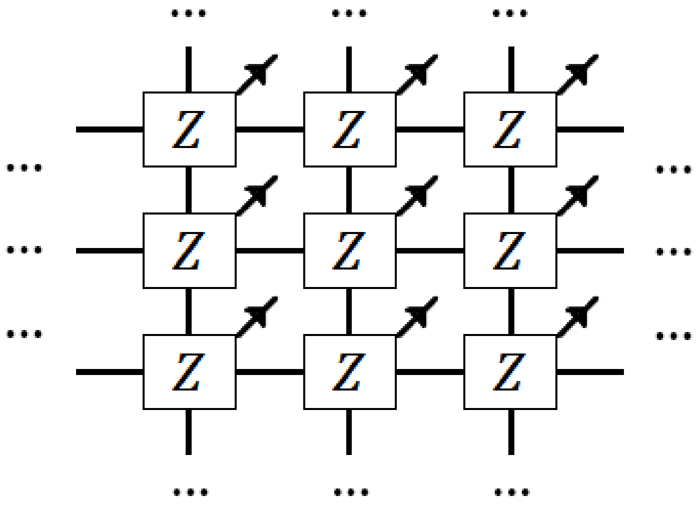

Figure 2.4: The diagram is a fragment of 2D 1-site unit cell Z PEPS, where the boundary is not specified and can be open, close, or periodic. In general, PEPS can admit other lattice structures such as the honeycomb shape and is not limited to one type of unit cell. The uncontracted edges are assigned with an out-pointing arrow to denote the ket indices.

sation constraint of a quantum state. Correspondingly, a n-dimensional TN lattice can be used to simulate a n-dimensional discrete quantum system.

On the other hand, MERA is distinct from MPS and PEPS in two ways[3]. Geometrically, MERA has an additional holographic dimension beside the edge state dimensions, see fig. 2.5 for more details. The extra dimension is measured by the scale parameter z, instead of the open edges, that generates the holographic geometry:

$$z \equiv \ln \lambda \tag{2.4}$$

where λ is a measure of the system size. For example, if the system size is e^{-n}, then $z = -n$, and the system size scales up exponentially as we approaches $z = 0$, where the physical legs locate. Meanwhile, a MERA is made of the isometric $\hat{u}^l_{ij}$ and disentangler $\hat{v}^{kl}_{ij}$ tensors , where both satisfy the unitary condition[20]:

$$\sum_{i,j} \hat{u}^l_{ij} \hat{u}^{\dagger ij}_{l'} = \delta^l_{l'} \tag{2.5}$$

$$\sum_{i,j} \hat{v}^{kl}_{ij} \hat{v}^{\dagger ij}_{k'l'} = \delta^{kl}_{kl'} \tag{2.6}$$

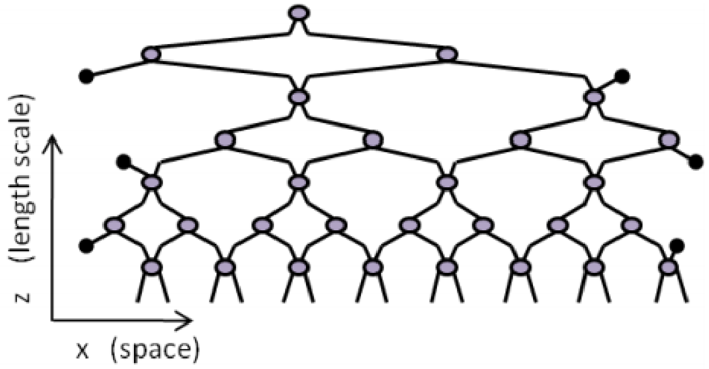

Figure 2.5: [3] The diagram is the illustration of the 1D MERA with a 2D holographic geometry. Beside the spatial dimension x, MERA has an extra length scale dimension z that measures the exponentially growing system size. In this example, the edge state serves as a hologram of the geometry of the total TN. The state is two dimensional because the number of open indices are proportional to the lattice area. The isometric tensor is the three legs tensor and disentangler is the four legs tensor in this diagram.

This constraint ensures the unit normalisation of the wave function. The isometric and disentangler can be understood as a renormalisation group transformation of the original quantum state from high energy to low energy, thus the unitary condition[20].

2.4 Schmidt Decomposition

In quantum information, the fundamental tool to calculating quantum entanglement entropy between a bipartite system is the Schmidt decomposition[21]. The Schmidt decomposition also plays a central role in the simulation of TNS. This method reveals all aspects of the entanglement entropy of the system of interest, thus helps to classify the type of the system – in our study, crucial for drawing a limit to quantum supremacy.

Given a Hilbert space of a MPS $\mathcal{H}$, it is possible to bipartite the system into two parts - the left and right MPS: $\mathcal{H} = \mathcal{H}_L \otimes \mathcal{H}_R$. In terms of the quantum state, we write[11]:

$$|\psi\rangle = \sum_{\alpha} R_\alpha \left|\alpha\right\rangle_L \otimes \left|\alpha\right\rangle_R \tag{2.7}$$

where $|\psi\rangle \in \mathcal{H}$ and $|\alpha\rangle_{L/R} \in \mathcal{H}_{L/R}$. Note that the basis states between the left and right *orthonormal basis states* need not share the same dimension, but the number of states that share a Schmidt coefficient must be the same. This ensures that the reduced density matrix between the left state and the right state is the same demanded by the conservation of information. From the Schmidt coefficient, we can determine the reduced density matrix via the contraction:

$$\begin{aligned}\rho^R &\equiv \mathrm{Tr}_L \left|\psi\right\rangle \left\langle\psi\right| \\ &= \sum_\alpha R_\alpha^2 \left|\alpha\right\rangle_R \left\langle\alpha\right|_R \end{aligned} \tag{2.8}$$

Thus, we can see that the square of the Schmidt coefficient are the diagonal entries of the reduced density matrix, and immediately from which, we can derive the entanglement entropy between the bipartite systems:

$$S = -\sum_\alpha R_\alpha^2 \ln R_\alpha^2 \tag{2.9}$$

In computing, given a many body quantum state (assume Einstein's summation):

$$\left|\rho\right\rangle = M_{n_1...n_k} \left|n_1...n_k\right\rangle \tag{2.10}$$

a bipartition is equivalent to reshaping the tensor $M_{n_1...n_k}$ into a $n \times m$ matrix:

$$M_{n_1...n_k} \left|n_1...n_k\right\rangle = \bar{M}_{ab} \left|ab\right\rangle \tag{2.11}$$

where the state $\left|n_1...n_i\right\rangle$ is mapped to $\left|a\right\rangle$ and the state $\left|n_{i+1}...n_k\right\rangle$ is mapped to $\left|b\right\rangle$. Calculation of the Schmidt coefficient is then equivalent to determining the singular value decomposition of the new matrix $\bar{M}_{ab}$, which is readily available to any programming language. However, in practice, SVD is computationally inefficient when dealing with many-body quantum problems, because the matrix $\tilde{M}_{ab}$ is in general very large. For 1-dimensional many-body quantum system, however, this is when the MPS comes in handy.

Chapter 3

The Matrix Product States

3.1 Definition and Basic Properties

In brief, a MPS is a chain of rank-3 tensors $A^{\sigma}_{a_1,a_2}$, with some kind of boundary $B^{\sigma}_{a_1}$, contracted with each other in the a_1, a_2 indices while keeping the index σ open to the state-vectors[22][11]:

$$|\psi\rangle = \sum_{\substack{a_1,\ldots,a_{n-1} \\ \sigma_1,\ldots,\sigma_n}} B^{\sigma_1}_{a_1} A^{\sigma_2}_{a_1,a_2} \ldots A^{\sigma_{n-1}}_{a_{n-2},a_{n-1}} B^{\sigma_n}_{a_{n-1}} |\sigma_1\sigma_2,\ldots,\sigma_{n-1},\sigma_n\rangle \tag{3.1}$$

The corresponding graphical representation can be found in fig. 3.1. Therefore, the open edges that contribute to what we can see are named physical legs and the contracted edges that contribute to the interactions between states the virtual or auxiliary legs. The boundary

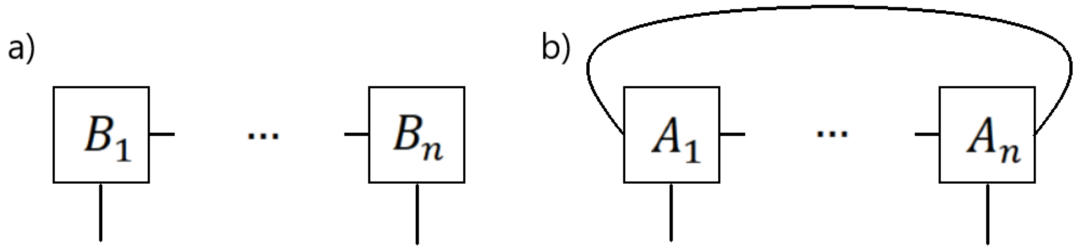

Figure 3.1: a) open boundary MPS; b) periodic boundary MPS. We can see that the uncontracted edge numbers is proportional to the length of the array in this case.

tensors need not exist. In this case, the MPS has an open boundary. If the boundary tensor connects to the first state to the final state, it is a periodic boundary condition. Otherwise, the boundary is closed.

MPS can be used to simulate one-dimensional quantum systems such as a spin chain with the nearest neighbour interaction, a one-dimensional array of cold atoms, where the individual site encodes information of the constituent quantum state — the individual spin or atoms. The virtual bond in this case would represent the interaction among the spins or cold atoms, and the physical legs are observable.

Now, we would like to look at why the MPS is so efficient[22]. Given a general tensor with n legs that features a d-level system, the number of parameters scales as $\mathcal{O}(d^n)$. For a MPS of N site, the total number of parameters scale as $\mathcal{O}(Nm^2d)$, where each matrix product operator(MPO) has m^2d parameters, m^2 for the virtual leg between the MPOs, and d for the physical leg. That is, as mentioned earlier, we store the site tensors without contracting them. However, the truth is contraction does take place, in times of calculating the correlation function for example, so whether MPS is efficient depends on the order of tensor contraction. A tensor data size scale exponentially $\mathcal{O}(e^n)$ with the number of uncontracted legs n of a tensor. Thus, the art of tensor contraction is the same as minimising the number of uncontracted legs.

3.1.1 Power of the Canonical Form

Another extremely useful aspect of MPS is that the MPS can be put into the so-called canonical form[12][23]. In brief, transforming to the canonical form is to transform the MPS basis state(eqn. 3.1) into the new orthonormal bases state in eqn. 3.12 such that the Schmidt values are easily obtained. For the sake of simplicity, we will study the canonical form of MPS with closed boundary condition. Given a bi-partition of the MPS between the i and $i+1$ site, the goal is to transform the left subregion into the so-called left canonical form and the right region to the left canonical form.

We start the construction of the *left canonical form* with a QR decomposition to the boundary tensor $B^{\sigma}_{a_1}$ in eqn. 3.1:

$$B^{\sigma_1}_{a_1} = \sum_{b_1} Q^{\sigma_1}_{b_1} R^{[1]}_{b_1,a_1} \tag{3.2}$$

such that the $R^{[1]}$ tensor is an upper triangle matrix and the Γ^{σ}_{b} tensor is "unitary" or "isometric" in the physical leg:

$$\sum_{\sigma} Q^{*\sigma}_{b} Q^{\sigma}_{c} = \delta_{b,c} \tag{3.3}$$

Next we want to decompose consecutive $A^{\sigma_2}_{a_1,a_2}$ to the form:

$$A^{\sigma_2}_{a_1,a_2} = \sum_{b_1,b_2} R^{-1[1]}_{a_1,b_1} Q^{\sigma_2}_{b_1,b_2} R^{[2]}_{b_2,a_2} \tag{3.4}$$

such that the first term on the RHS is the inverse of $R^{[1]}$, $R^{[2]}$ is again upper triangle and $Q^{\sigma_2}_{b_1,b_2}$ is "isometric":

$$\sum_{\sigma,b} Q^{*\sigma}_{bm} Q^{\sigma}_{bn} = \delta_{mn} \tag{3.5}$$

Now the left canonical form reads:

$$\sum_{\substack{b_1,\ldots,b_i\\ \sigma_1,\ldots,\sigma_i}} Q^{\sigma_1}_{b_1} Q^{\sigma_2}_{b_1,b_2} \ldots Q^{\sigma_i}_{b_{i-1},b_i} R^{[i]}_{b_i,a_i} \left|\sigma_1,\ldots,\sigma_i\right\rangle \tag{3.6}$$

Analogously, starting with the right boundary tensor and the consecutive tensors, we can use the LQ decomposition to obtain the *right canonical form*[1]:

$$\sum_{\substack{b_{i+1},\ldots,b_n\\ \sigma_{i+1},\ldots,\sigma_n}} L'^{[i+1]}_{a_{i+1},b_{i+1}} Q'^{\sigma_{i+1}}_{b_{i+1},b_{i+2}} \ldots Q'^{\sigma_{n-1}}_{b_{n-1},b_n} Q'^{\sigma_n}_{b_n} \left|\sigma_{i+1},\ldots,\sigma_n\right\rangle \tag{3.7}$$

Combining the left and right canonical forms, we can write $|\psi\rangle$ as the so-called *mixed canonical*

---

[1] the definitions of L' and Q' in the LQ decomposition are completely analogous to that of the QR except everything now is in reversed order, and the matrix L' is now lower triangular matrix

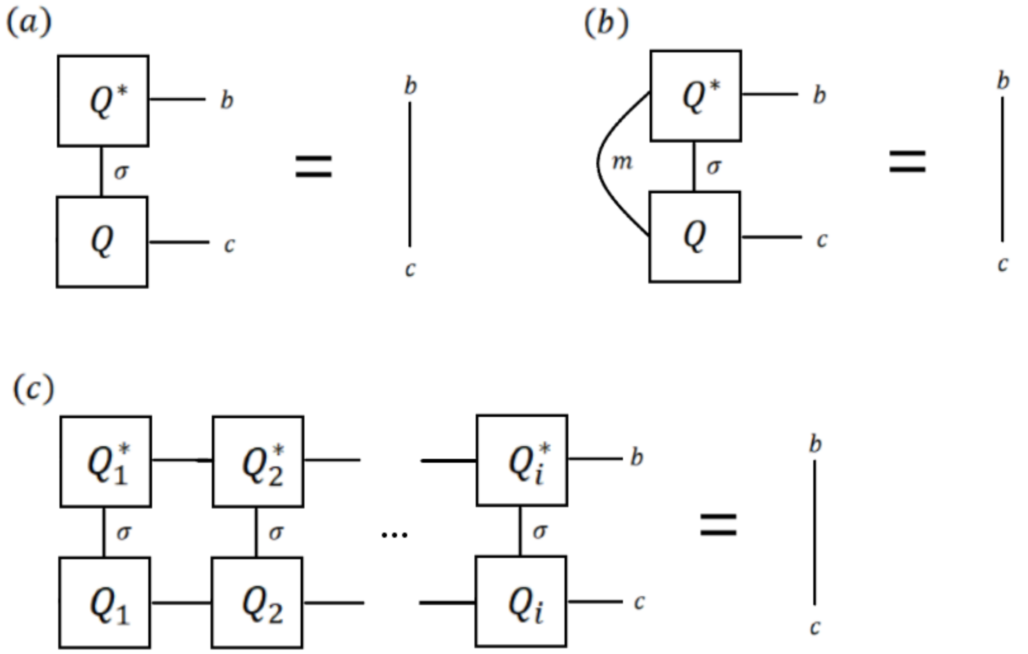

Figure 3.2: a) represents the isometric property of $Q^{\sigma_1}_{b_1}$ in its canonical form. Straight line on the RHS represents $\delta_{m,n}$ b) represents the isometric property of $Q^{\sigma_i}_{b_{i-1},b_i}$. Combining properties a) and b), we can show in c) that the left canonical form must be an orthonormal basis. We can perform the same calculation for the right canonical form to find that they also represent the orthonormal basis. Note that Q^* represent the Hermitean conjugate of Q here.

form:

$$\begin{aligned}
&\sum_{\substack{b_1,\dots,b_n\\ \sigma_1,\dots,\sigma_n\\ a}} Q^{\sigma_1}_{b_1}\dots Q^{\sigma_i}_{b_{i-1},b_i}\left(R^{[i]}_{b_i,a}L'^{[i+1]}_{a,b_{i+1}}\right)Q'^{\sigma_{i+1}}_{b_{i+1},b_{i+2}}\dots Q'^{\sigma_n}_{b_n}\left|\sigma_1,\dots,\sigma_i\right\rangle\left|\sigma_{i+1},\dots,\sigma_n\right\rangle\\
&=\sum_{\substack{b_1,\dots,b_n\\ \sigma_1,\dots,\sigma_n\\ m,n}} Q^{\sigma_1}_{b_1}\dots Q^{\sigma_i}_{b_{i-1},b_i}\left(U^{\dagger}_{b_i,m}S_{m,n}U'_{n,b_{i+1}}\right)Q'^{\sigma_{i+1}}_{b_{i+1},b_{i+2}}\dots Q'^{\sigma_n}_{b_n}\left|\sigma_1,\dots,\sigma_i\right\rangle\left|\sigma_{i+1},\dots,\sigma_n\right\rangle\\
&=\sum_{m,l} S_{m,l}\left|m\right\rangle_L\left|l\right\rangle_R \qquad (3.8)
\end{aligned}$$

where we redefine:

$$\left|m\right\rangle_L=\sum_{b_1,..,b_i,m} Q^{\sigma_1}_{b_1}\dots Q^{\sigma_i}_{b_{i-1},b_i}U^{\dagger}_{b_i,m}\left|\sigma_1,\dots,\sigma_i\right\rangle \qquad (3.9)$$

$$\left|l\right\rangle_R=\sum_{l,b_{i+1}\dots b_n} U'_{l,b_{i+1}}Q'^{\sigma_{i+1}}_{b_{i+1},b_{i+2}}\dots Q'^{\sigma_n}_{b_n}\left|\sigma_{i+1},\dots,\sigma_n\right\rangle \qquad (3.10)$$

In the second step, we perform an singular value decomposition to the $R^{[i]}_{b_i,a}L^{[i+1]}_{a,b_{i+1}}$ to obtain the diagonal matrix $S_{m,n}$ that encodes the Schmidt values. There are several observations to make on the canonical form. Readers can check that $|m\rangle_L$ and $|l\rangle_R$ are the orthonormal basis on their own due to the properties of the isometric Q^σ tensors, a graphical proof is given in fig. 3.2. It means that eqn. 3.9 and 3.10 in fact represent the Schmidt basis of the MPS state. Secondly, $S_{m,n}$ has a dimension that of the virtual legs (bonding dimension) - the entropy of the MPS not bounded by the physical leg size as what we would naively expect. Therefore, we have just shown that MPS must always follow an area law if the bond dimension is bounded from above – entanglement entropy is proportional to the number of bonds the connects the bipartite subsystem. However, the converse is not true – even if the bond dimension is not bounded from above, it is still possible to recover the area law, and we will illustrate that in the single fibre loop set-up.

Computationally speaking, the algorithm to obtain the Schmidt values involves only individual QR and LQ decompositions on the site tensor. Therefore, we can calculate the entanglement entropy while avoid generating the MPS wave function; this is precisely why the literature mentions that the number of parameters needed to specify the TNS scales linearly for MPS, as mentioned in the beginning.

As mentioned earlier, every one-dimensional system has an MPS representation regardless of the property of the entanglement entropy, but paradoxically, the MPS architecture must follow the area law given a bounded bonding dimension. Therefore, whether a finite bonding dimension can capture the physics of the 1D system determines whether the 1D system is classically easy to simulate. In TNS theory, the approximation of the quantum system by a fixed virtual leg dimension is called the truncation of the bonding dimension. In particular, a quantum system is classically easy to simulate if for any truncation error $\epsilon > 0$, which measures the error of the approximated MPS, there exist a finite bonding dimension χ such that[24]:

$$\left| |\psi\rangle - \sum_{\alpha=0}^{\chi} S_\alpha |\alpha\rangle_L \otimes |\alpha\rangle_\alpha \right| = \left| \sum_{\alpha=\chi+1}^{\chi_{\max}} S_\alpha |\alpha\rangle_L \otimes |\alpha\rangle_R \right| = \sum_{\alpha=\chi+1}^{\chi_{\max}} S_\alpha^2 < \epsilon \tag{3.11}$$

where $\chi \le \chi_{\max} < \infty$. The question of classical simulability then becomes a classification problem of the density matrix. This is the fundamental reason why entanglement entropy is useful for determining the hardness of a simulation.

Thus far, I have reviewed the most efficient construction method of the mixed canonical form. However, the definition of the *full canonical form* (or the *canonical form*) is as follow:

$$|\psi\rangle = \sum_{a} \Gamma^{\sigma_1}_{a_1} S^{[1]}_{a_1 a_1'} \Gamma^{\sigma_2}_{a_1' a_2} S^{[2]}_{a_2 a_2'} \dots \Gamma^{\sigma_{n-1}}_{a_{n-1}' a_n} S^{[n-1]}_{a_n a_n'} \Gamma^{\sigma_n}_{a_n'} |\sigma_1 \dots \sigma_n\rangle \tag{3.12}$$

where $S^{[i]}_{a_i,a_i'}$ is the diagonal matrix that contains the Schmidt coefficient, the boundary $\Gamma^{\sigma_{1/n}}_{a_{1/n}}$ are isometric analogous to eqn. 3.3, and the bulk $\Gamma^{\sigma_i}_{a_{i-1}' a_i}$ satisfy the property:

$$\sum_{\sigma_i, c, a_{i-1}', b_{i-1}'} \left(S^{[i-1]}_{c b_{i-1}'} \Gamma^{\sigma_i}_{b_{i-1}' m} \right)^* S^{[i-1]}_{c a_{i-1}'} \Gamma^{\sigma_i}_{a_{i-1}' n} = \delta_{mn} \tag{3.13}$$

$$\sum_{\sigma_i, c, a_i, b_i} \left(\Gamma^{\sigma_i}_{m b_i} S^{[i]}_{b_i c} \right)^* \Gamma^{\sigma_i}_{n a_i} S^{[i]}_{a_i c} = \delta_{mn} \tag{3.14}$$

That is, multiplying the left Schmidt coefficient to the Γ tensor gives the left canonical form, and right gives the right canonical form. One may question the existence of such Γ tensor, but it is possible to construct the full canonical form from eqn. 3.8 via systematically applying QR and LQ decomposition; the derivation can be found in the appendix. Intuitively speaking, the canonical form is a change in the basis state of the virtual legs such that the entanglement information between any bipartitions of the MPS is explicitly manifested. In other words, the canonical form is a gauge transformation that simplifies calculations.

Another powerful feature of the canonical form is that it simplifies the calculation of the correlation function of a local operator. Due to the orthogonality of the site tensors, sites that are out of the range of the local operator naturally vanishes, as shown in fig. 3.3. In the analysis, advantages of the canonical form are exploited to reduce the computational cost.

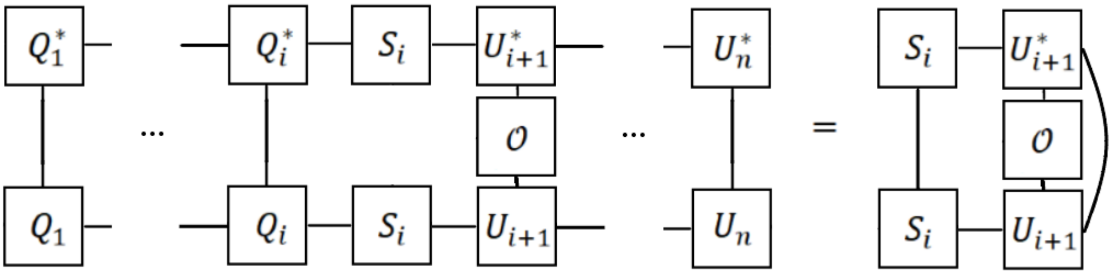

Figure 3.3: In the canonical form, the Schmidt basis cancels itself. Calculation of the expectation $\langle\mathcal{O}\rangle$ requires only the contraction of the local indices. Since the canonical form does not alter the physical legs, there is no need to transform the operator basis state for the contraction.

3.1.2 Limit of Canonical Form

Thus far, we have introduced the MPS as a one-dimensional TNS. In this representation, the TNS is a chain of lattice sites. We show that it is possible to transform the lattice site into a canonical form where calculations are massively simplified. As we shall see, the canonical form is also fundamental to our analysis of time-bin quantum optics.

However, when we want to describe TNS with loops, the canonical form decomposition becomes less useful[2]. Consider a MPS where the boundary tensor $B_{a_1}^{[0]\sigma_1}$ and $B_{a_1}^{[n]\sigma_1}$ becomes the bulk tensor $A_{a_1,a_2}^{[0]\sigma_2}$ and $A_{a_1,a_2}^{[n]\sigma_2}$, such that $A_{a_1,a_2}^{[0]\sigma_2}$ is connected to $A_{a_1,a_2}^{[n]\sigma_2}$. There are three observations to make:

- The original QR decomposition scheme no longer decomposes the MPS into a canonical form.
- Suppose there exists a canonical decomposition for the periodic MPS where the site tensors satisfy eqns. (3.13) and (3.14), the corresponding "Schmidt values" for a bipartition no longer makes sense because applying a single cut to a loop results in a connected line. For a periodic MPS, we need at least two cuts to define a bipartition, and that corresponds to two "Schmidt values" in the canonical decomposition.
- Suppose we calculate the "Von-Neumann entropy" from the two selected "Schmidt values", the resulting entropy is not the entanglement entropy because the Schmidt basis

---

[2] in practice it is possible to approximate periodic MPS with open , smooth, or infinite boundary condition[25][26].

are not orthogonal.

Although the "Schmidt values" of a periodic MPS do not give us the entanglement entropy, we can show that the "Von-Neumann entropy" represents the upper bound of the entanglement entropy because the mutual information is non-0, and a graphical explanation is shown in fig. 3.4. Thus, canonical decomposition only returns us approximation of the physical quantities of the periodic MPS, when attempting to calculating its entanglement entropy and correlation functions.

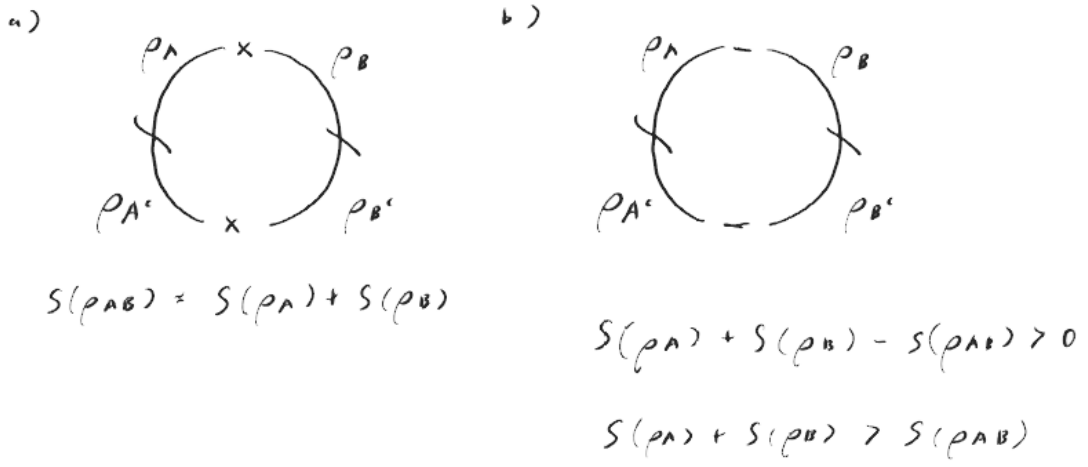
a)
ρ_A
ρ_B
ρ_{A^c}
ρ_{B^c}
$S(\rho_{AB}) = S(\rho_A) + S(\rho_B)$
b)
ρ_A
ρ_B
ρ_{A^c}
ρ_{B^c}
$S(\rho_A) + S(\rho_B) - S(\rho_{AB}) > 0$
$S(\rho_A) + S(\rho_B) > S(\rho_{AB})$

Figure 3.4: A brief argument why the canonical decomposition is useful in giving the upper bound of the entanglement entropy. a) Consider a direct product system $A \cup A^c \otimes B \cup B^c$. Applying cuts to $A \cup A^c$ and $B \cup B^c$ in the middle simultaneously gives the product density matrix $\rho_{AB} = \rho_A \rho_B$, and thus the corresponding entanglement entropy $S(\rho_A) + S(\rho_B)$. b) Now we introduce entanglement between $A \cup A^c$ and $B \cup B^c$, then the mutual information, defined as the LHS of the first line, is > 0, so the entanglement entropy is smaller than the sum of the entanglement entropy of ρ_A and ρ_B. Back to periodic MPS, the singular values are precisely where the cuts located.

3.2 Time Evolving Block Desimation (TEBD)

Given a MPS in its canonical form, we can efficiently compute its time-evolution. The technique is known as Time-Evolving Block Decimation[13], and it is consisted of two parts:

- Trotter-Suzuki decomposition[27]

- Time evolution

Trotter-Suzuki approximates unitary evolution of the full system for small time δt as local unitary evolutions between the neighbouring sites via decomposing the parent Hamiltonian into multiple parts that are compatible to the MPS formalism. Intuitively, this decomposition is possible because at a small interval of time the time evolution of a lattice is local. The approximation essentially takes the locality literally by ignoring the higher order contribution by the non-neighbour interactions, after taking the small time interval limit. Take the spin-1/2 XXZ chain of size L with nearest neighbour interaction Hamiltonian as an example:

$$\hat{H} = \sum_{i=1}^{L} \frac{1}{2}\left(\hat{S}_i^{+}\hat{S}_{i+1}^{-} + h.c.\right) + g\hat{S}_i^{z}\hat{S}_{i+1}^{z} = \sum_{i=1}^{L} \hat{h}_{i,i+1} \tag{3.15}$$

We can decompose the model into a even and a odd part:

$$\begin{aligned} \hat{H}_e &= \sum_{i \text{ even}}^{L} \frac{1}{2}\left(\hat{S}_i^{+}\hat{S}_{i+1}^{-} + h.c.\right) + g\hat{S}_i^{z}\hat{S}_{i+1}^{z} \\ \hat{H}_o &= \sum_{i \text{ odd}}^{L} \frac{1}{2}\left(\hat{S}_i^{+}\hat{S}_{i+1}^{-} + h.c.\right) + g\hat{S}_i^{z}\hat{S}_{i+1}^{z} \end{aligned} \tag{3.16}$$

We can approximate the time evolution with the Baker-Campbell-Hausdorff formula:

$$e^{i\hat{H}\delta t} \approx e^{i\hat{H}\delta t + \frac{1}{2}[\hat{H}_e,\hat{H}_o]\delta t^2} = e^{i\hat{H}_e\delta t}e^{i\hat{H}_o\delta t} \tag{3.17}$$

Due to the condition of locality:

$$[\hat{h}_{i,i+1}, \hat{h}_{j,j+1}] = 0 \text{ if } i \neq j-1, j, j+1 \tag{3.18}$$

the summands in the even/odd Hamiltonian commute with each other - internally commuting:

$$e^{i\hat{H}_e\delta t} = e^{i\delta t \sum_{i \text{ even}} \hat{h}_{i,i+1}} = \prod_{i \text{ even}} e^{i\hat{h}_{i,i+1}\delta t} \tag{3.19}$$

Thus, unitary operation of $\hat{H}_e$ on a MPS can be decomposed into unitary operation of $\hat{h}_{i,i+1}$ on site $i, i+1$. Under this approximation, the original parent unitary operation is decomposed into sequence of even and odd local site operations - a huge improvement to the computational cost. The error of this approximation is of second order $\mathcal{O}(\delta t^2)$. Consider time evolution t, which takes $\frac{t}{\delta t}$ computational steps to reach. The accumulated error rate is $\frac{t}{\delta t}\mathcal{O}(\delta^2) = \mathcal{O}(\delta)$ - thus the name first-order TEBD (TEBD1). Since the first order error is an anti-commutator, it can be eliminated via the symmetrisation:

$$\begin{aligned} e^{i\frac{1}{2}\hat{H}_e\delta t}e^{i\hat{H}_o\delta t}e^{i\frac{1}{2}\hat{H}_e\delta t} &= e^{i(\frac{1}{2}\hat{H}_e+\hat{H}_o)\delta t+\frac{1}{4}[\hat{H}_e,\hat{H}_o]\delta t^2}e^{i\frac{1}{2}\hat{H}_e\delta t} + \mathcal{O}(\delta t^3) \\ &= e^{i\hat{H}\delta t+\frac{1}{4}[\hat{H}_e,\hat{H}_o]\delta t^2+\frac{1}{4}[\hat{H}_o,\hat{H}_e]\delta t^2} + \mathcal{O}(\delta t^3) \\ &= e^{i\hat{H}\delta t} + \mathcal{O}(\delta t^3) \end{aligned} \tag{3.20}$$

and thus, we obtain the second-order TEBD (TEBD2) immediately from the first. We can apply the same strategy by looking at the commutators in the higher order terms in the Baker-Campbell-Hausdorff formula to construct the high order TEBD. Now lets include the next nearest neighbour term to the original Hamiltonian:

$$\hat{H}' = \lambda\sum_{i=1}^{L}\frac{1}{2}\left(\hat{S}_i^+\hat{S}_{i+2}^- + h.c.\right) + \frac{1}{2}\hat{S}_i^z\hat{S}_{i+2}^z \tag{3.21}$$

The generalised Trotter-Suzuki approximation divides the new Hamiltonian into three internally commuting Hamiltonian:

$$\begin{aligned} \hat{H}_1 &= \sum_{i \mod 3=1}^{L}\hat{h}_{i,i+1} + \hat{h}'_{i,i+2} \\ \hat{H}_2 &= \sum_{i \mod 3=2}^{L}\hat{h}_{i,i+1} + \hat{h}'_{i,i+2} \\ \hat{H}_3 &= \sum_{i \mod 3=0}^{L}\hat{h}_{i,i+1} + \hat{h}'_{i,i+2} \end{aligned} \tag{3.22}$$

The TEBD1:

$$e^{i\hat{H}_{\text{new}}\delta t} = e^{i\hat{H}_1\delta t}e^{i\hat{H}_2\delta t}e^{i\hat{H}_3\delta t} \tag{3.23}$$

and the TEBD2:

$$
\begin{aligned}
e^{i\frac{1}{2}\hat{H}_1\delta t}e^{i\frac{1}{2}\hat{H}_2\delta t}e^{i\hat{H}_3\delta t}e^{i\frac{1}{2}\hat{H}_2\delta t}e^{i\frac{1}{2}\hat{H}_1\delta t} &= e^{i\frac{1}{2}(\hat{H}_1+\hat{H}_2)\delta t+i\frac{1}{4}[\hat{H}_1,\hat{H}_2]\delta t^2}e^{i\hat{H}_3\delta t}e^{i\frac{1}{2}(\hat{H}_1+\hat{H}_2)\delta t-i\frac{1}{4}[\hat{H}_1,\hat{H}_2]\delta t^2} \\
&+ \mathcal{O}(\delta t^3) \\
&= e^{i\frac{1}{2}(\hat{H}_1+\hat{H}_2)\delta t}e^{i\hat{H}_3\delta t}e^{i\frac{1}{2}(\hat{H}_1+\hat{H}_2)\delta t} + \mathcal{O}(\delta t^3) \\
&= e^{i(\hat{H}_1+\hat{H}_2+\hat{H}_3)\delta t} + \mathcal{O}(\delta t^3) \qquad (3.24)
\end{aligned}
$$

In the second equality, the second order commutator vanishes because they cancel out each other and the commutator between $\hat{H}_3$ and $[\hat{H}_1, \hat{H}_2]$ is a third order contribution. Inductively, for a $n-1$-th neighbour interaction, the Trotter-Suzuki approximation splits the original Hamiltonian into n internally commuting parts with TEBD1 and TEBD2 as follow:

$$
\begin{aligned}
U(\delta t)^{\hat{T}EBD1} &= e^{i\hat{H}_1\delta t}e^{i\hat{H}_2\delta t}...e^{i\hat{H}_n\delta t} + \mathcal{O}(\delta t^2) \\
U(\delta t)^{\hat{T}EBD2} &= e^{i\frac{1}{2}\hat{H}_1\delta t}e^{i\frac{1}{2}\hat{H}_2\delta t}...e^{i\hat{H}_n\delta t}...e^{i\frac{1}{2}\hat{H}_2\delta t}e^{i\frac{1}{2}\hat{H}_1\delta t} + \mathcal{O}(\delta t^3) \qquad (3.25)
\end{aligned}
$$

After decomposing the time-evolution operator into local terms, we can act the local unitary operator individually onto sites covered by the operator. In TEBD, a one-step time evolution on all sites is consisted of four main parts, see fig. 3.5 for further details:

- Starting with the canonical form, contraction of neighbouring virtual bonds to form a time-evolution block
- Local unitary time evolution
- SVD of the block back to a canonical form
- Repeat the process for the rest of the sites

As promised in the introduction, the all powerful canonical form plays a crucial role in TEBD; the data structure allows SVD of the block tensor and thus the reason why local unitary operation is implementable on a MPS. A proof is attached in the Appendix to show that SVD

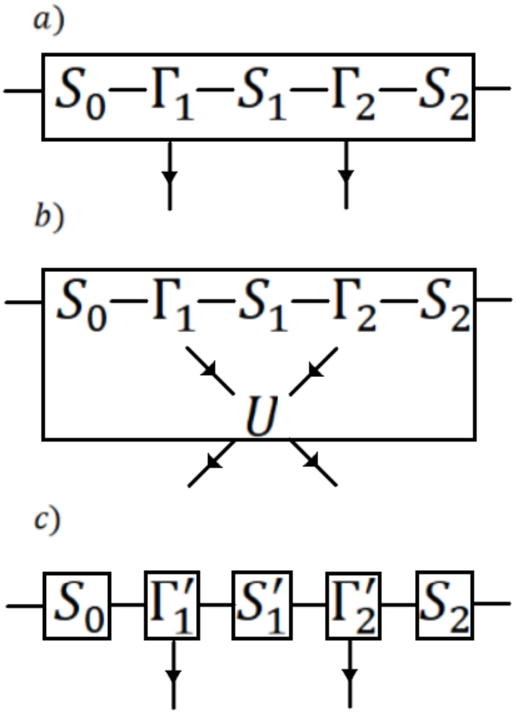
a)
S_0 Γ_1 S_1 Γ_2 S_2
b)
S_0 Γ_1 S_1 Γ_2 S_2
U
c)
S_0 Γ'_1 S'_1 Γ'_2 S_2

Figure 3.5: a) contract site tensors that are involved in a local time evolution together. b) time evolution. c) SVD to obtain the new singular values and site tensors. Bonds within the retangular box are contracted and otherwise left untouched.

preserves the canonical form. In this project, the TEBD algorithm is used to simulate the boson sampling to study the entanglement entropy property.

Chapter 4

Conservation Law of TNS

4.1 Abelian Charge Conservation

I suppose one of the most interesting and useful features of TNS is the conservation law in TNS. Conservation law appears naturally in the framework of TNS, essentially because the tensors indices are quantum numbers, and quantum numbers are always associated with conserved quantities. Computationally, it is possible to further reduce the number of parameters further by conservation law via transforming into a suitable basis state in the physical legs[28][29][17][30][31]. The basic idea is analogous to the angular momentum selection rule in between atomic energy level.

4.1.1 Examples

Let's consider a (first-order) dipole transition, the selection rule guarantees that an odd wave function can only transform to an even wave function due to the odd parity of the dipole operator. To define odd and even parity wave-function, we can assign parity information with the operator $\hat{P}$ to each of the atomic quantum states:

$$\langle n, l, m| \hat{P} |n, l, m\rangle = (-1)^l \tag{4.1}$$

where l is the total angular momentum, m is the angular momentum projection and n is the energy quantum number. In the language of TNS, we say that each quantum number n, l, m represents a leg, because a generic atomic wave function is represented as (Einstein summation):

$$|\psi\rangle = M_{nlm} |n, l, m\rangle \tag{4.2}$$

where M_{nlm} is a rank-3 tensor with its indices defined by three legs n, l, m. Meanwhile the charge information of the parity is defined via the exponent of the parity: Charge(l) $= l$ mod 2.

The angular momentum selection rule is manifested in the dipole moment:

$$\langle n', l', m'| q\hat{x} |n, l, m\rangle \tag{4.3}$$

Since the operator $\hat{x}$ carries the charge $+1$(mod2), the transition is non-0 only if the parity of the incoming leg $|l\rangle$ and the outgoing leg $\langle l'|$ add up to $+1$(mod2), and this is how we implement selection rules in the TNS. The dipole transition exemplifies how to encode charge information of a discrete symmetry into a TNS operator. In general, it is possible to define $\mathbb{Z}_n$ charge theoretically for a tensor operator and the corresponding leg that defines the symmetry.

Selection rule is not limited to discrete symmetry but also continuous ones. Now we consider the $U(1)$ charge rule. The total charge of an operator $\hat{O}$ depends on how the generator $\hat{H}$ commutes with $\hat{O}$:

$$[\hat{H}, \hat{O}] = q\hat{O} \tag{4.4}$$

For example, lets consider a 2-level raising and lowering operators $S_{\pm}$. Since, relative to the spin projection S_z, it admits a commutation relation:

$$[S_z, S_{\pm}] = \pm S_{\pm} \implies e^{-iS_z\theta} S_{\pm} e^{+iS_z\theta} = e^{\pm i\theta} S_{\pm} \tag{4.5}$$

$S_{\pm}$ has a charge value of ± 1 relative to the spin projection operator. In the spin basis $\{|\uparrow\rangle, |\downarrow\rangle\}$, each state-vector carries a charge:

$$\mathrm{Charge}(|\uparrow\rangle) = 1/2 \tag{4.6}$$

$$\mathrm{Charge}(\langle\uparrow|) = -1/2 \tag{4.7}$$

$$\mathrm{Charge}(|\downarrow\rangle) = -1/2 \tag{4.8}$$

$$\mathrm{Charge}(\langle\downarrow|) = 1/2 \tag{4.9}$$

Conjugation of the state-vector sends the charge to negative simply because the dual vector transforms as:

$$e^{i\theta} |\uparrow\rangle \xrightarrow{conjugate} \langle\uparrow| e^{-i\theta} \tag{4.10}$$

$|\uparrow\rangle$ and $\langle\downarrow|$ together carries a charge of 1, and vice versa, thus:

$$\begin{cases} \langle\uparrow| S_+ |\downarrow\rangle |\uparrow\rangle \langle\downarrow| = |\uparrow\rangle \langle\downarrow| , \\ \langle\downarrow| S_- |\uparrow\rangle |\downarrow\rangle \langle\uparrow| = |\downarrow\rangle \langle\uparrow| , \\ \text{otherwise} = 0 \end{cases} \tag{4.11}$$

As demonstrated, the total charge of the basis, $|\uparrow\rangle \langle\downarrow| , |\downarrow\rangle \langle\uparrow|$ always matches the operator charge. In matrix representation:

$$S_+ = \begin{bmatrix} 0 & 1 \\ 0 & 0 \end{bmatrix}, S_- = \begin{bmatrix} 0 & 0 \\ 1 & 0 \end{bmatrix} \tag{4.12}$$

Note that this statement is not true if we choose other set of bases such as $\{|+\rangle , |-\rangle\}$. That is, only if we gauge the TNS in the right manner in the beginning of the simulation, we can minimise the number of non-0 entries in the tensor operators. We can also apply this reasoning to quantum fields operators:

$$[\hat{N}, \hat{a}_p^\dagger] = \hat{a}_p^\dagger \tag{4.13}$$

$$[\hat{N}, \hat{a}_p] = -\hat{a}_p \tag{4.14}$$

where

$$\begin{cases} \langle n| \hat{a_p}^\dagger |n-1\rangle = \sqrt{n} \\ \langle n-1| \hat{a_p} |n\rangle = \sqrt{n} \\ \text{otherwise} = 0 \end{cases} \tag{4.15}$$

In this example, the quantum number is the bosonic occupancy of momentum p, we can see that the bases of the raising operator – $|n\rangle\langle n-1|$ – must always have charge $n-(n-1)=1$ and $(n-1)-n=-1$ for the bases of the lowering operator – $|n-1\rangle\langle n|$. In fact, the commutator in eqn. 4.5 is equivalent to eqns. 4.13 and 4.14. Thus, in both examples demonstrates the $U(1)$ charge conservation law. The difference between the $U(1)$ charge versus the Z_n charge is that the $U(1)$ quantum numbers $\in \mathbb{Z}$ while the Z_n quantum numbers $\in Z_n$.

4.1.2 Abelian Charge Selection Rule

The generalised selection rule (or the Abelian charge rule) states that: For a tensor $M_{i_1 \ldots i_n}$ in the eigen-basis of the charge, and a set of indices $\{a_1, ..., a_n\}$ where $a_k \in i_k$[24]:

$$\forall \{a_1, ..., a_n\}, \sum_k \eta(a_k) q(a_k) \neq Q(M_{i_1 \ldots i_n}) \implies M_{a_1 \ldots a_n} = 0 \tag{4.16}$$

where $q(a_k)$ is the charge of the quantum number a_k, and:

$$\eta(a_k) = \begin{cases} 1 \text{ if } a_k \text{ belongs to } |a_k\rangle \\ -1 \text{ if } a_k \text{ belongs to } \langle a_k| \end{cases} \tag{4.17}$$

Given a general tensor, and a good basis, then we can also calculate the total charge of tensor from the leg charge information.

We proceed on further by proving the generalised selection rules for the Abelian internal symmetry. The proof procedure is analogous to [29]. Let $\hat{T}_{i_1 \ldots i_n}$ be a rank-(n, m) tensor. Then the tensor transforms like eqn. 2.1. Let the operator has Abelian charge q ((mod$n$) if symmetry is

$\mathbb{Z}_n$), then it must transform as:

$$M_{i_1}^{j_1}...M_{i_n}^{j_1}M_{l_1}^{k_1}...M_{l_m}^{k_m}\hat{T}_{j_1...j_n}^{l_1...l_m} = e^{-iqx}\hat{T}_{i_1...i_n}^{k_1...k_m} \tag{4.18}$$

where $x \in \mathbb{R}$ if the symmetry is $U(1)$ and $x \in \mathbb{Z}$ if the symmetry is $\mathbb{Z}_n$. In general, this kind of transformation is called covariant. Since each individual indices in the tensor corresponds to a quantum number, we can transform the quantum number to the eigen-basis of the charge $\{|0\rangle, |1\rangle, ..., |q\rangle, ...\}$, and they transform as:

$$|q_i\rangle \rightarrow e^{-iq_i x}|q_i\rangle \tag{4.19}$$

subsequently the tensor transforms as:

$$M_{i_1}^{j_1}...M_{i_n}^{j_1}M_{l_1}^{k_1}...M_{l_m}^{k_m}\hat{T}_{j_1...j_n}^{l_1...l_m} = e^{-iq_{i_1}x}...e^{-iq_{i_n}x}e^{iq_{k_1}x}...e^{iq_{k_m}x}\hat{T}_{i_1...i_n}^{k_1...k_m} \tag{4.20}$$

Comparing eqn. 4.18 and 4.20, we get the charge rule of the tensor:

$$e^{-iq_{i_1}x}...e^{-iq_{i_n}x}e^{iq_{k_1}x}...e^{iq_{k_m}x} = e^{-iqx} \tag{4.21}$$

In the literature, covariant and invariant tensors are called symmetric.

4.2 Abelian Charge Summation Rule in TNS

Now that we understand the charge rule of individual tensor operator, we can further investigate the charge structure of a general TNS.

Consider the simplest example - a direct product between two tensor, $A \otimes B$. Given that A, a rank $(1,1)$ tensor, has charge a and B, a rank $(0,2)$ tensor, has charge b with respect to the parameter θ, the evolution of the direct product state is then $e^{(a+b)\theta}A \otimes B$. Thus, the new tensor has charge $a+b$. Subsequently we will show that the charge must be additive for two tensors despite of the tensor contraction. Consider a tensor $C_{ik} = A_i^j B_{jk}$, and an instant of indices $a \in i, b \in j, c \in k$. Contraction ensures that charges in the j entries must cancel out because the $\eta(b) = -1$ for A and $\eta(b) = 1$ for B, so the total charge of C is:

$$\begin{aligned} Q(C) &= \eta(a)q(a) + \eta(c)q(c) \\ &= (q(a) - q(b)) + (q(b) + q(c)) \\ &= Q(A) + Q(B) \end{aligned} \tag{4.22}$$

This expression immediately generalises for any contractions between tensors of all ranks. Therefore, the total charge of a TNS is just the sum of the charges of the constituent operators.

4.3 Non-Abelian Charge Conservation

As we see from the previous section, Abelian symmetry can reduce the number of parameter in the TNS once we identify the right basis where selection rule can be implemented. As for non-Abelian symmetry, the philosophy is similar in that we can identify the right basis to implement the selection rule, but non-Abelian symmetry has an additional feature where a tensor can be represented as a direct sum of irreducible representations by a change of basis. It further imposes a contraints on the non-0 parameters via the irreducible representations[31].

In the Abelian case, we can assign arbitrary charge that takes integer value to a rank (n, m) tensor, because all Abelian irreps are 1D, such that the tensor product or contracted states are trivial ($1 \otimes 1 = 1$), and additive. In the non-Abelian case, however, each irreps corresponds to the transformation property of a tensor with a fixed rank, so it is not possible to assign to a tensor an arbitrary irrep. Instead, we need the Clebsch-Gordan coefficients to determine the transitions of irreps. after tensor contractions.

To define the charge data for TNS in a non-Abelian symmetry G, we need 3 types of quantum numbers[1][17][31]: charge q that defines the dimension of one irrep., t that determines the degeneracies of q, q_z the *z-label* as generalisation of the spin-projection operator. A general rank-$3n$ tensor $\hat{T}$ in G is then represented in this charge basis:

$$(\hat{T}_{q_1,q_2,\ldots,q_n})_{(t_1,t_2,\ldots,t_n),(q_{1z},q_{2z},\ldots,q_{nz})} \tag{4.23}$$

The charge q is associated with the Casmir operators $\hat{C}_\gamma$ that commute with all generators $\hat{G}_\sigma$ of a Lie group[]:

$$[\hat{C}_\gamma, \hat{G}_\sigma] = 0 \tag{4.24}$$

For example, in $SU(2)$, the Casmir operator is the total angular momentum operator $\hat{S}$ that returns the value $\sqrt{l(l+1)}$, in general there are $N-1$ Casmir operators for $SU(N)$. In practice, however, we find that $q \equiv \max\{q_z\}$.

Meanwhile, the charge q_z is associated with the generators $\hat{H}_\alpha$ in the Cartan subalgebra. That is, the maximal set of mutually commuting generators of the Lie algebra:

$$[\hat{H}_\alpha, \hat{H}_\beta] = 0 \tag{4.25}$$

4.3.1 Property of Operator with Charge q_1

With the above information, we can define an irreducible operator $\hat{F}^{q_1}_{q_{1z}}$ to be an operator that is an irreducible representation of charge q_1. Analogous to eqn. 4.4, the *z-label* charge of $\hat{F}^{q_1}_{q_{1z}}$ can be found:

$$[\hat{H}_\alpha, \hat{F}^{q_1}_{q_{1z}}] = q_{1z_\alpha}\hat{F}^{q_1}_{q_{1z}} \tag{4.26}$$

where $\hat{H}_\alpha$ are the Cartan generators. For example, the spin projection commutation relation in eqn. 4.5. From an irreducible operator, we can contruct the so-called irreducible operator set $\{\hat{F}^{q_i}_{q_{iz}}\}$ (IROPs) through the raising and lower operators:

---

[1] actually, there can be degeneracies within the q_z number as well due to the group symmetry, and it is known as the inner multiplicity.

$$[\hat{G}_\alpha, \hat{F}^{q_1}_{q_{1z}}] = g^{[\alpha]}_{q_{1z},q_z} \hat{F}^{q_1}_{q_z} \tag{4.27}$$

For example, $\{\hat{S}^+, \hat{S}_z, \hat{S}^-\}$ is an irreducible operator set for the adjoint representation in $SU(2)$. Note that an IROP is rank-$(2,2)$, where the 2s denotes the pair (qq_z), because the charge of the IROP is defined. Each irreducible operator corresponds to one dimension, so the number of all operators is the dimension of the representation.

4.3.2 Non-Abelian Charge Structure of a TNS

Constructing non-Abelian charge information of a TNS is like playing with legos. Thus, we need to identify the lego blocks first. Given two representations $H^{[q_1]}$ and $H^{[q_2]}$ with state-space $|q_1, q_{1z}\rangle$ and $|q_2, q_{2z}\rangle$, the tensor product state read $|q_1, q_{1z}; q_2, q_{2z}\rangle$. If the product state is reducible, then it can be decomposed to a direct sum of irreps:

$$H^{[q_1]} \otimes H^{[q_2]} = \bigoplus_{p_i} H^{[p_i]} \tag{4.28}$$

While the Young Tableau informs us of the new irreps.[32], we need the Clebsch-Gordan coefficient (CGC)[2], $\langle q_f, \vec{q}_{fz} | q_1, \vec{q}_{1z}; q_2, \vec{q}_{2z}\rangle$, to obtain information on the transition amplitude for the tensor product $|\vec{q_1}; \vec{q_2}\rangle$:

$$|q_1, q_{1z}; q_2, q_{2z}\rangle = \sum_{f,fz} \langle q_f, q_{fz} | q_1, q_{1z}; q_2, q_{2z}\rangle \, |q_f, q_{fz}\rangle \tag{4.29}$$

In tensor network, CGC is represented as a rank-$(2,4)$ tensor with two input legs and one output leg, as shown in fig. 4.1.

With CGC, we can now simplify IROP $\hat{F}^{q_1}_{q_{1z}}$ with through the Wigner-Eckart Theorem:

$$\langle q't; q'_z| \, \hat{F}^{q_1}_{q_{1z}} \, |qt; q_z\rangle = \langle q't| \, \hat{F}^{q_1} \, |qt\rangle \, \langle q' q'_z | q_1 q_{1z}; q q_z\rangle \tag{4.30}$$

---

[2] Clebsch-Gordan coefficient, as the name suggested, can be determined by the Clesch-Gordan decomposition. Inner multiplicity is included in the coefficient if symmetry has degeneracy in the z-label.

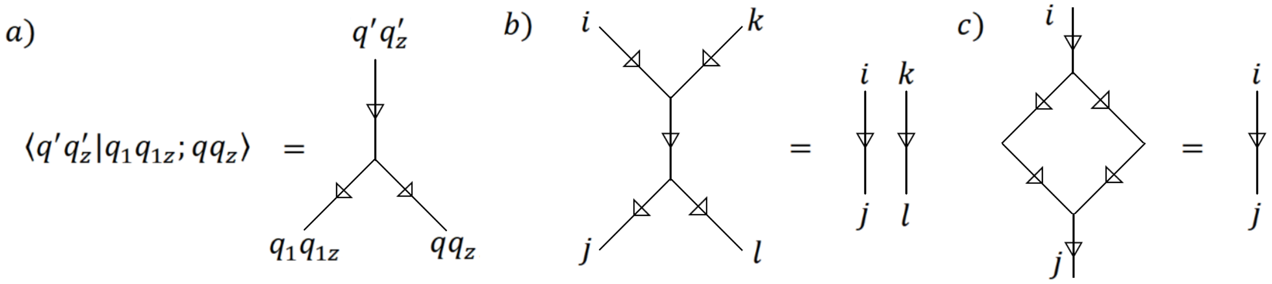

Figure 4.1: a) is the TN representation of CGC. The intersection is where the tensor locates. b), c) are the orthonormal conditions of CGC, where the straight line(s) denotes the Kronecker deltas. The pair (q, q_z) is compactly written as i. The connected edge is a tensor contraction between two CGCs. In finite-dimensional Hilbert space, either b) or c) must be a projection operator, but not applicable here.

where t is the degeneracy of q, and $\langle q't|\, \hat{F}^{q_1}\, |qt\rangle$ is called the reduced matrix element. $\hat{F}^{q_1}_{q_{1z}}$ must be a product of CGC element because it acts like the state space $|q_1; q_{1z}\rangle$ due to the charge constraints:

$$\hat{H}_\alpha \hat{F}^{q_1}_{q_{1z}} |q; q_z\rangle = [\hat{H}_\alpha, \hat{F}^{q_1}_{q_{1z}}] |q; q_z\rangle + \hat{F}^{q_1}_{q_{1z}} \hat{H}_\alpha |q; q_z\rangle = (q_{1z} + q_z)\hat{F}^{q_1}_{q_{1z}} |q; q_z\rangle \tag{4.31}$$

$$\hat{H}_\alpha |q_1 q_{1z}; qq_z\rangle = |\hat{H}_\alpha q_1 q_{1z}; qq_z\rangle + |q_1 q_{1z}; \hat{H}_\alpha qq_z\rangle = (q_{1z} + q_z) |q_1 q_{1z}; qq_z\rangle \tag{4.32}$$

Again $\hat{F}^{q_1}_{q_{1z}}$ is rank-$(2, 2)$ with a direct product decomposition that separates the z-labels from the degeneracy indices; however, the theorem actually applies to reducible operators as well because the theorem holds true for any $(q_1 q_{1z})$ pairs. In other words, $\langle q't; q'_z|\, \hat{F}^{q_1}_{q_{1z}}\, |qt; q_z\rangle$ can in fact be rank-$(2, 4)$.

Suppose now the operator is invariant under in the symmetry, i.e. $q_1 = 0$, then we obtain the factorisation:

$$\langle q't; q'_z|\, \hat{F}^0_0\, |qt; q_z\rangle = \langle q't|\, \hat{F}^0\, |qt\rangle\, \delta_{q',q}\delta_{q'_z,q_z} \tag{4.33}$$

In this example, the Kronecker deltas are trivial and in simulation we only need to store information of $\langle q't|\, \hat{F}^0\, |qt\rangle$. Again Wigner-Eckart theorem is a decomposition for tensor of rank-$(2, 4)$ or lower. It captures how non-Abelian symmetry simplifies the tensor. The direct product expression implies that the tensor must be sparse (more 0s entries than non-0), and only the reduced matrix element is needed to be stored for calculation, given that the CGC is worked out in advanced.

For tensor network with 4 × 2 + 2 indices, we can write, with the same line of reasoning:

$$\begin{aligned}\langle q't; q'_z| \hat{F}^{q_1}_{q_{1z}} \hat{F}^{q_2}_{q_{2z}} |qt; q_z\rangle &= \sum_{pp_z} \langle q't; q'_z| \hat{F}^{q_1}_{q_{1z}} |p; p_z\rangle \langle p; p_z| \hat{F}^{q_2}_{q_{2z}} |qt; q_z\rangle \\ &= \sum_{p} \langle q't| \hat{F}^{q_1} |p\rangle \langle p| \hat{F}^{q_2} |qt\rangle \left[\sum_{p_z} \langle q'q'_z|q_1 q_{1z}; pp_z\rangle \langle pp_z|q_2 q_{2z}; qq_z\rangle\right]\end{aligned} \tag{4.34}$$

where the CGC satisfies the following identity:

$$\langle q'q'_z|q_1 q_{1z}; q_2 q_{2z}; qq_z\rangle = \sum_{p,p_z} \langle q'q'_z|q_1 q_{1z}; pp_z\rangle \langle pp_z|q_2 q_{2z}; qq_z\rangle \tag{4.35}$$

That is, the new relationship is no longer a direct product expression, and there are internal charge degrees of freedom p to sum over because the reduced element is not p independent. For a general decomposition of tensor $\hat{T}^{q_1 q_2}_{q_{1z} q_{2z}}$, we can perform SVD to the tensor to insert the extra momentum pp_z degrees of freedom. The tensor network representation is shown in fig. 4.2. A general tensor decomposition reads[3]:

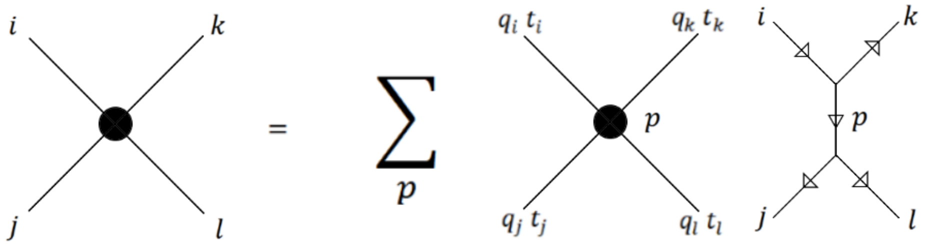

Figure 4.2: This is the generalisation of Wigner-Eckart theorem to tensor with 4 legs. The (i, j, k, l) indices denotes the pair (qq_z), while p is just the charge label. It can be shown that the tensor can be decomposed into the reduced matrix element with 5 legs and a CGC network. Such decomposition remains valid for tensors with n legs.

$$\begin{aligned}&\langle q't; q'_z| (\hat{T}^{q_1,q_2,\ldots,q_n})_{(t_1,t_2,\ldots,t_n),(q_{1z},q_{2z},\ldots,q_{nz})} |qt; q_z\rangle \\ &= \sum_{p_1,\ldots,p_k} \langle q't| (\hat{T}^{q_1,q_2,\ldots,q_n})_{(t_1,t_2,\ldots,t_n),(p_1,\ldots,p_k)} |qt\rangle \sum_{p_{1z},\ldots,p_{kz}} \text{CGC network}\end{aligned} \tag{4.36}$$

---

[3] The CGC network is otherwise known as the spin network in the $SU(2)$ case.

where k is the number of internal charges. Thus, a general tensor network is decomposed into a sum of reduced tensor network and a CGC network due to the non-Abelian symmetry! CGC and the Wigner-Eckart Theorem are the lego pieces that we need! Comparing this result to the Abelian case, we immediately realise that the Wigner-Eckart theorem is just a generalisation to the Abelian charge conservation because the CGC in the Abelian case is just a Kronecker delta:

$$\langle q_1, q_2, ..., q_n | q_1', q_2', ..., q_n' \rangle = \delta_{(q_1+q_2+...+q_n),(q_1'+q_2'+...+q_n')} \tag{4.37}$$

Readers might notice that there is no unique way to construct the CGC network. For example, in fig. 4.2, we can exchange the j and k indices and the overall outcome should not be affected. It can be shown that different arrangements of the arrows are related by the so-called *F-move*. The F-move is important to relating different CGC networks, and find applications in spin network and string-net models[33][34][35]. Non-Abelian charge conservation rule in TNS involves some profound mathematical frameworks. However, this piece of mathematics is out of the scope of this review, so it will not be further discussed.

Chapter 5

Bosonic Quantum Circuit

5.1 Motivation

Recently, some attention are paid to the simulation of many-mode quantum optical set-up beyond the phase space formalism characterised by the Wigner function[36][37]. An example of a many-mode quantum optical system is featured by an assembly of the beam-splitters that splits and couples multiple photon modes together as the photons travel down the path. While the phase space formalism might be insufficient in describing the many-mode system, TNS seems to be a promising candidate to work around that problem because beam-splitters operation seems to follow the area law in certain settings. Therefore, a technique such as truncation of the bonding dimension might be useful helpful in improving the simulation.

On the other hand, we have entered the so-called Noisy Intermediate-Scale Quantum (NISQ) era[1] where noisy quantum simulation devices are readily available for real-life application. Researchers are eager to find out the extent to which NISQ devices demonstrate quantum supremacy. MPS becomes the perfect language to determine the extent to which noise undermines quantum supremacy because TNS allows a direct measure of the entanglement entropy of the noisy system. There have been a few attempts to determine the effects of noises on and simulation hardness of boson sampling device[2][38][39]. This direction, therefore, motivates this dissertation to study the entropy property of bosonic quantum circuits with TNS.

We should also take note of how TNSs are traditionally used - as a variational ansatz state to seek for the ground state of a particular many-body set-up or as an initial state such that the final state can be determined via the TEBD. Meanwhile, the building blocks of a traditional TNS are individual sites with a local Hamiltonian that describes the site's time evolution under no interaction.

When it comes to modeling beam splitter set-up with TNS however, its philosophy is different from the traditional method. Instead of sites, the building block of the TNS is now unitary operators. The architecture of a quantum optical TNS is best understood as a quantum circuit instead of a lattice. The concept of locality persists in TNS description of a quantum optical system - local Hamiltonian is replaced by local unitary operator - but the changes will lead to a new entanglement structure in quantum optics, as our analysis will show.

5.2 Tensor Representation of Beam-Splitter

The Beam Splitter operator, also called the bosonic hopping operator, is understood as a map from two annihilation operators to two annihilation operators[37]:

$$U : \mathcal{H}_{\hat{a}_1} \otimes \mathcal{H}_{\hat{a}_2} \to \mathcal{H}_{\hat{b}_1} \otimes \mathcal{H}_{\hat{b}_1} \tag{5.1}$$

$$\begin{bmatrix} \hat{a}_1 \\ \hat{a}_2 \end{bmatrix} \to e^{\theta(\hat{a}^\dagger \hat{b} - \hat{b}^\dagger \hat{a})} \begin{bmatrix} \hat{a}_1 \\ \hat{a}_2 \end{bmatrix} e^{-\theta(\hat{a}^\dagger \hat{b} - \hat{b}^\dagger \hat{a})} = \begin{bmatrix} \cos\theta & -\sin\theta \\ \sin\theta & \cos\theta \end{bmatrix} \begin{bmatrix} \hat{a}_1 \\ \hat{a}_2 \end{bmatrix} = \begin{bmatrix} \hat{b}_1 \\ \hat{b}_2 \end{bmatrix} \tag{5.2}$$

where the coupling matrix is an matrix element of the $SO(2)$ symmetry. This representation is elegant because it avoids writing out the full state space basis which is unbounded from above. However, in TNS it is necessary to construct a state space representation, and in state space basis the beam splitter operator takes the form[40]:

$$R^{(n_1,n_2)}_{N_1,N_2} = (-1)^{N_2} \left(\frac{N_1!}{N_2! n_1! n_2!} \tau^{-(N_1-n_2)} (1-\tau)^{-N_1-n_1} \right)^{1/2} \frac{d^{N_2}}{d\tau^{N_2}} [\tau^{n_1} (1-\tau)^{n_2}] \tag{5.3}$$

where n_1, n_2 are the input photons, N_1, N_2 are the output, and τ is the transmission coefficient defined as $\tau = \cos^2\theta$. Since the beam splitter operator conserves the total number of particles, it exhibits a $U(1)$ symmetry and has charge 0. We can then apply the charge conservation rule as explained in Chapter 4 to narrow down the allowed transition:

$$R^{(n_1,n_2)}_{N_1,N_2} \neq 0 \iff N_1 + N_2 = n_1 + n_2 \tag{5.4}$$

5.3 Entanglement Entropy by a Single Beam Splitter

Now we study the entanglement property of beam splitter as the simplest instance of the TNS, this also allow readers to familiarise how the Fock space description works in quantum optics. Initially, we send two photons $\hat{a}_2^\dagger$ and $\hat{a}_1^\dagger$ into the beam splitter to couple them together:

$$|11\rangle = \hat{a}_2^\dagger \hat{a}_1^\dagger |0\rangle \tag{5.5}$$

The beam splitter that we adopted changes the state to:

$$\begin{aligned} \hat{a}_2^\dagger \hat{a}_1^\dagger |0\rangle &\to \left(\cos\theta \hat{a}_2^\dagger - \sin\theta \hat{a}_1^\dagger\right)\left(\sin\theta \hat{a}_2^\dagger + \cos\theta \hat{a}_1^\dagger\right)|0\rangle \\ &= \frac{\sin 2\theta}{\sqrt{2}}\left(|20\rangle - |02\rangle\right) + \cos 2\theta\, |11\rangle \end{aligned} \tag{5.6}$$

Partial tracing the the pure state over the $\hat{a}_2$ basis, the reduce density matrix reads:

$$\frac{\sin^2 2\theta}{2}\left(|0\rangle\langle 0| - |2\rangle\langle 2|\right) + \cos^2 2\theta\, |1\rangle\langle 1| \tag{5.7}$$

and thus the entanglement entropy:

$$S(\hat{\rho}_{\hat{a}_1}) = \sin^2 2\theta \log\frac{\sin^2 2\theta}{2} + \cos^2 2\theta \log\cos^2 2\theta \tag{5.8}$$

Reader may notice at this point that the reduced density matrix is diagonal (i.e. lack of coherence). In fact, the reduced density matrix of a beam splitter is *always* diagonal because the output photon number is conserved, meaning that for $|mn\rangle$ and $|m'n'\rangle$:

$$m \neq m' \iff n \neq n' \tag{5.9}$$

Meanwhile, because the reduced density matrix is always diagonal and positive definite, we realise that entanglement entropy is bounded from above by the number of photons in the system:

$$S(\hat{\rho}_{\hat{a}_1}) \leq \log{(N+1)} \tag{5.10}$$

This bound describes the bound of one leg in the tensor representation of the coupling device. For a generalised architecture of a photon coupling device with multiple output legs, we would also expect that the entanglement entropy is bounded roughly by the sum of $\ln(N_{\text{leg}}+1)$ number of photons at each leg. Thus, given an one dimensional output of quantum circuit, area law is not guaranteed. It is interesting then to ask the question how to classify area law quantum circuit states from non area law quantum circuit states.

5.4 Photonic Quantum Information Encoding

In linear quantum optics, there are four ways to encode quantum information - polarisation state, spatial mode, time-bin mode, and frequency mode information encoding[41].

For polarisation qubits, the quantum state is a linear sum of the polarisation orthogonal basis - the left $|l\rangle$ and right $|r\rangle$ circular polarized states. Mathematically, we can map all polarisation to the Poincare sphere in the same manner as the Bloch sphere for two qubits. For spatial modes, superposition happens in a coupling device and the output state is spread across different locations on a basis of for example photon occupancy. For time-bin modes, interference also happens at a coupling device but the output state is in time-order. Meanwhile, frequency mode creates a quantum state with frequencies as the basis state.

At first, we will focus on time-bin information encoding. In particular, we study a kind of coupling device called the fibre loop where the input time-bin mode would couple themselves in a time order manner. Due to this unique structure, it is found that such kind of coupling device admits an MPS structure in the time dimension. In the following sections, I will define the time-bin operators that constitute the MPS.

5.4.1 Single and Multiple Fibre Loops

Single fibre loop is an experimental technique to implement mode mixing between adjacent temporal modes via a temporal delay of the previous mode. The advantage of this technique is that the same experimental set-up can be used multiple times during an experiment. While a single fibre loop is a static coupler, an arbitrary interferometer can be implemented if the coupler is variable - important for quantum Fourier Transform[37]. Still, it is interesting to know the complexity of a static coupler such as the single fibre loop.

As illustrated in fig. 5.1, the one-loop architecture will lead to a time-ordered unitary operation on the initial time-bin modes, and such time-ordered structure is precisely an MPS architecture. The natural question to ask is whether this MPS follows the area law.

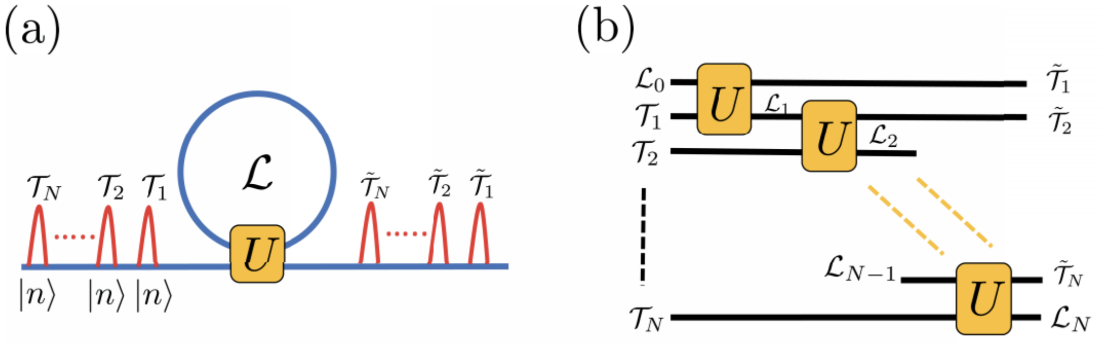
(a)
$\mathcal{L}$
$\mathcal{T}_N$
$\mathcal{T}_2$
$\mathcal{T}_1$
$\tilde{\mathcal{T}}_N$
$\tilde{\mathcal{T}}_2$
$\tilde{\mathcal{T}}_1$
U
$|n\rangle$
$|n\rangle$
$|n\rangle$
(b)
$\mathcal{L}_0$
$\mathcal{T}_1$
$\mathcal{T}_2$
$\mathcal{T}_N$
U
$\mathcal{L}_1$
U
$\mathcal{L}_2$
$\tilde{\mathcal{T}}_1$
$\tilde{\mathcal{T}}_2$
$\mathcal{L}_{N-1}$
U
$\tilde{\mathcal{T}}_N$
$\mathcal{L}_N$

Figure 5.1: a) Experimental set-up of the single fibre loop, where N time-bin modes $\mathcal{T}_i$ are sent regularly to the loop $\mathcal{L}$, resulting in mixing via the unitary operator U among the modes and complexity in the N output modes $\tilde{\mathcal{T}}_i$; b) Quantum circuit representation of the set-up, where the fibre loop is represented as a ladder of unitary operations between every adjacent time-bin modes.

The first observation we make is the property of the individual operator. For simplicity, we represent the individual unitary operator U as the intersection of the line, and the inverse U^{-1} also as the intersection but with an opposite orientation indicated by the arrow. Then, the unitary condition simply reads: Such results have two consequences. First, the MPS

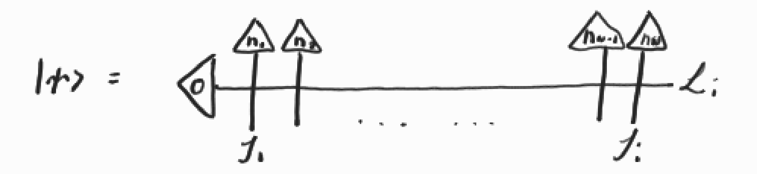

Figure 5.2: This is the MPS representation of the single fibre loop. This representation is equivalent to b) in fig. 5.1 in the sense that the operation order of U and thus the relative entanglement structure is not changed by deforming b) to the MPS representation here. This is indeed the power of categorical quantum mechanics.[4]

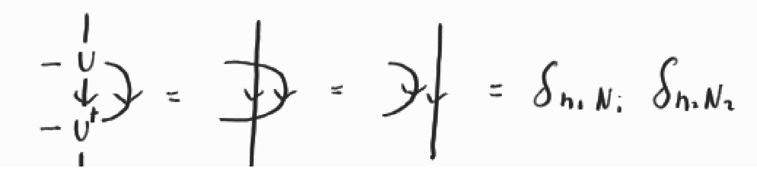

Figure 5.3: This is the TN representation of unitarity of the beam splitter operator. The unitary operator has outgoing arrows whilst its inverse has incoming arrows. Diagrammatically, it is a statement on the topological property of the four legs unitary operators, that is, the equivalence of intersecting and non intersecting lines. The resulting non-intersected lines represent the two Kronecker deltas.

always has unit norm, as shown in fig. 5.4. This is nice because quantum circuit should not change the normalisation of the initial product state: The second consequence is that the

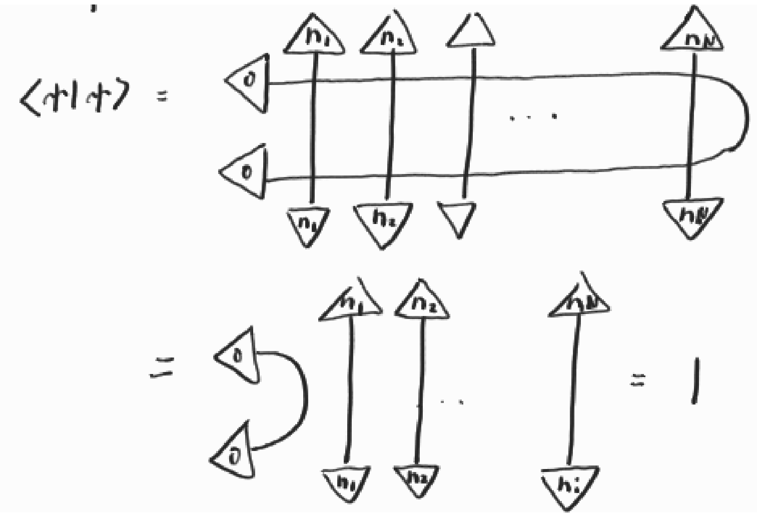

Figure 5.4: To calculate the normalisation with tensor network, we just need to iteratively unintersects the time-bin lines, $|n_1\rangle, |n_2\rangle, ..., |n_N\rangle$ and the loop line $|0\rangle$. The third equality is trivially obtained because $\langle n|n\rangle$=1

right subspace side of the bipartite MPS is naturally in a canonical form, as shown in fig. 5.5. This is an important insight because it means that the future time-bin operations always contribute nothing to the entanglement entropy. Therefore, the entanglement entropy between

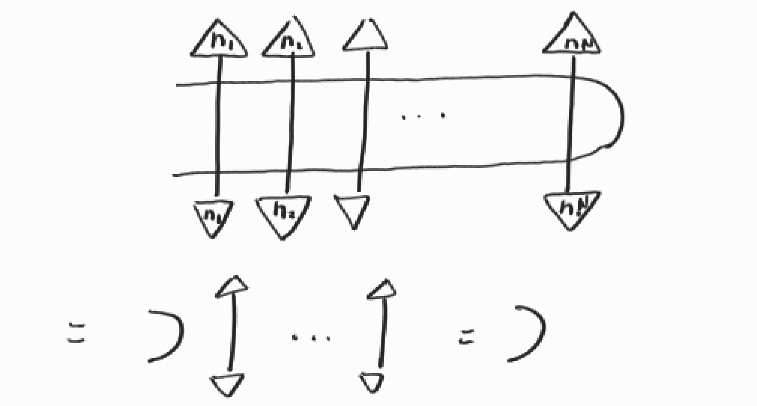

Figure 5.5: Contraction the right side of the MPS immediately gives the Kronecker delta, meaning that the future operation, the future output time bin mode relative to the ith bipartition is already in a canonical form.

the bipartite time bin modes is equal to the entanglement entropy between the loop state and the past output time-bin modes. It is equivalent to saying that the loop state always bound the entanglement entropy.

We can immediately generalise this proof to show that the future time-bin modes in any fibre loop architecture must have their entropy bounded by the loop state. We can generalise that for any fibre loop architecture, the corresponding quantum circuit consists of two types of state, the output time-bin modes as the physical legs, and the loop states that connect the detectable output time-bin modes as the virtual legs in a time order manner. Thus, for any kind of fibre loop set-up, it satisfies the following relationship in fig. 5.6. In this kind of fibre loop architecture, the tensor network state is between time-bin modes is always connected in a time-ordered manner. Thus, when we bipartite the generalised MPS into two part, the right side never contributes to the entanglement for the same reason as for the single fibre loop case, see fig. 5.7.

Although the entanglement entropy for a generalised fibre loop set-up is bounded by the loop state, the loop states can have occupancy that is unbounded from above. The next step is to show the occupancy is not a problem. We know that the entanglement entropy of the loop state is maximised in thermal equilibrium because the loop state is in an open system (that is, the particle number of the loop state is not conserved). Thus, the reduced density matrix of

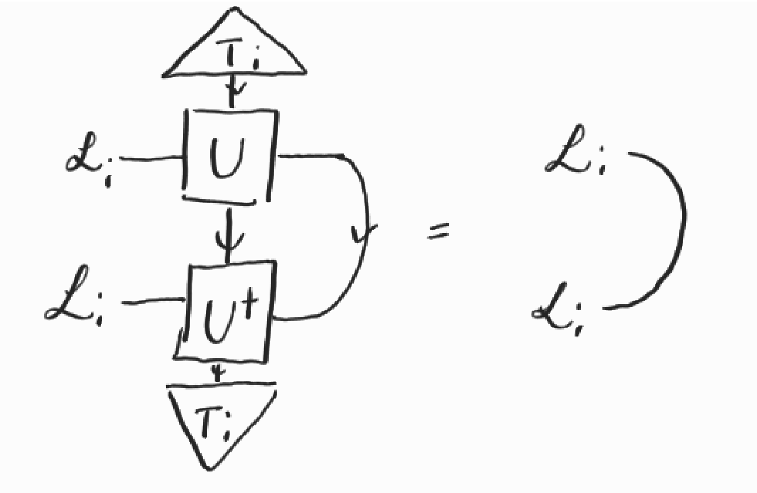

Figure 5.6: This diagram is the generalised representation of fibre loops set-up in a multi-fibre loops scenarios. The time-bin modes vector T_i represents a collection of initial time-bin modes, and $\mathcal{L}_i$ similarly represents a collection of loop states. The unitary operator here is understood as a collection of local beam-splitter operators. Indeed, a collection of unitary operators is still unitary. Thus, in the generalised set-up, so the identity property of the unitary operator is still satisfied. However, identity is now over the composite initial loop state basis.

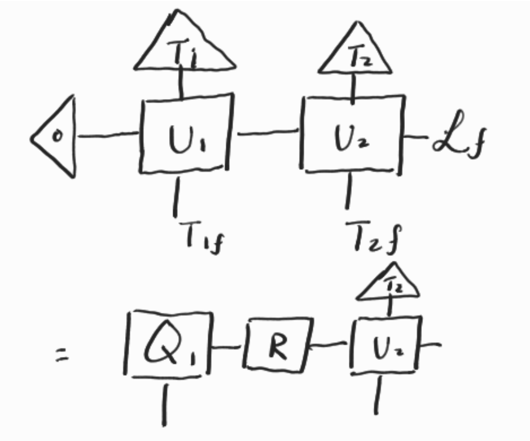

Figure 5.7: Putting the generalised MPS into the canonical form, and the right side never contributes to the QR decomposition.

the loop state is described by the Gibbs state[42]:

$$\hat{\rho} = \frac{e^{-\hat{H}/k_B T}}{\operatorname{Tr} e^{-\hat{H}/k_B T}} \tag{5.11}$$

In our study, we only send one mode into the linear optical set-up, thus the following partition function:

$$Z = \operatorname{Tr} e^{-\hat{H}/k_B T} = \sum_{n=0}^{\infty} e^{-n\epsilon/k_B T} = \frac{1}{1 - e^{-\epsilon/k_B T}} \tag{5.12}$$

In diagonal basis of the occupancy n, we find that:

$$\hat{\rho} = \sum_{n=0}^{\infty} \frac{e^{-n\epsilon/k_B T}}{1 - e^{-\epsilon/k_B T}} \left|n\right\rangle \left\langle n\right| \tag{5.13}$$

However, this is not a very useful density matrix because there is no well-defined Hamiltonian in our set-up. Luckily, we can rewrite the expression in terms of the mean occupancy:

$$\bar{n} = \frac{\sum_{n=0}^{\infty} n e^{-n\epsilon/k_B T}}{Z} = -k_B T \frac{\partial_\epsilon Z}{Z} = -k_B T \partial_\epsilon \ln Z = \frac{1}{e^{\epsilon/k_B T} - 1} \tag{5.14}$$

Rearranging, we get the density matrix in thermal equilibrium:

$$\hat{\rho} = \frac{1}{\bar{n}+1} \sum_{n=0}^{\infty} \left(\frac{\bar{n}}{\bar{n}+1}\right)^n \left|n\right\rangle \left\langle n\right| \tag{5.15}$$

Thus, the Von-Neumann entropy:

$$\begin{aligned}
S &= -\operatorname{Tr} \hat{\rho} \ln \hat{\rho} \\
&= -\sum_{n=0}^{\infty} \frac{1}{\bar{n}+1} \left(\frac{\bar{n}}{\bar{n}+1}\right)^n \ln \frac{1}{\bar{n}+1} \left(\frac{\bar{n}}{\bar{n}+1}\right)^n \\
&= \sum_{n=0}^{\infty} -\frac{1}{\bar{n}+1} \left(\frac{\bar{n}}{\bar{n}+1}\right)^n (n \ln \bar{n} - (n+1) \ln(\bar{n}+1)) \\
&= (1+\bar{n}) \ln(1+\bar{n}) - \bar{n} \ln \bar{n}
\end{aligned} \tag{5.16}$$

In the last equality, we make use of the fact that:

$$\sum_{n=0}^{\infty} \frac{1}{\bar{n}+1} \left(\frac{\bar{n}}{\bar{n}+1}\right)^n n = \bar{n} \tag{5.17}$$

For a single fibre then, we expect the entanglement entropy to be bounded by eqn. 5.16. For multiple loop states architecture, we expect that the entanglement entropy to be bounded by the sum of the upper bounds of the loop state entanglement entropy because of the triangular inequality[43]:

$$S_{\mathcal{L}_i} + S_{\mathcal{L}_{i+1}} \geq E_{\mathcal{L}_i} + E_{\mathcal{L}_{i+1}} \geq E_{\mathcal{L}_i, \mathcal{L}_{i+1}} \tag{5.18}$$

where $S_{\mathcal{L}_i}$ denotes the upper bound of the ith loop state, $E_{\mathcal{L}_i}$ the entropy of ith loop state, and $E_{\mathcal{L}_i,\mathcal{L}_{i+1}}$ the total entanglement entropy of both ith and $i+1$th loop states. We find the generalised analytical upper bound:

$$E_{\text{total loop state}} \leq \sum_i (1+\bar{n}_i)\ln(1+\bar{n}_i) - \bar{n}_i \ln \bar{n}_i \tag{5.19}$$

where $\bar{n}_i$ is the average photon number in the ith loop state. Now we proceed to derive the condition when the generalised analytical upper bound is fixed. For a single fibre loop, the average photon number in time step i is given by:

$$n(i) = \cos^2(\theta)n(i-1) + \sin^2(\theta)n_i \leq \max(n(i-1), n_i) \tag{5.20}$$

where $n(i-1)$ is the mean photon in the previous step and n_i is the input photon number in time i. Expanding the recursive relation to get:

$$n(i) \leq \max(n_1, ..., n_i) \tag{5.21}$$

That is, if the input photon number has a maximum, then the average photon number is bounded from above, and thus the loop state entanglement entropy. Thus, despite any multiple loop state architectures, the entanglement entropy must be bounded from above as long as the sequence of input time-bin modes has a maximal photon number. That concludes our proof that any loop-state architecture must eventually follow the area law.

Consequence of the Area Law for arbitrary fibre loop architectures

In quantum circuits, there are in general two ways to apply local quantum gates to the initial states: sequential and parallel operations [11]. Quantum Fourier transform is an example of sequential quantum circuit structure; boson sampling device is an example of parallel quantum circuits. Sequential operation induces a strict casual order between the input states; parallel application of local operators will construct a quantum circuit with a partial order structure. Meanwhile, a sequential circuit has a causal sequence.

The area law proof procedure we elucidated for sequential operation of beam splitter operators applies to sequential operations of any quantum gates. In fact, for bounded quantum numbers (such as qubits) the proof is easier because we do not need to worry about the unbounded occupancies.

Although sequential quantum circuit always follows an area law, it by no means implies that that multiple loop architecture is easy to simulate. In a sequential gate operation, the hardness of the simulation depends on the individual gate operation. Back to eqn. 5.19, assuming that $\bar{n}_i$ is fixed across different loop states, then we realise that the analytical upper bound scales linearly as we introduce more fibre loops. A linear rise of entanglement entropy implies exponential growth of the Hilbert space. Meaning that it is exponentially hard for a classical computer to scale up the number of fibre loops in a simulation.

5.4.2 Boson Sampling Bosonic Circuit

We have proved that the sequential bosonic circuit must always follow the area law, although the upper bound can be so high that the circuit is hard to simulate. Now we turn our attention to boson sampling to see what complexity it produces. Following the previous analysis, We study the tensor network for boson sampling for its entanglement.

Consider a boson sampling device of size N, next we want to compute the entanglement entropy between subsystem of A and $\bar{A}$ of size M and $N - M$. Analogous to the previous analysis, we exploit unitarity to explore which part of the boson sampling device contributes to the entanglement entropy. We can achieve that via constructing the density matrix of the subsystem A from the sampling pure state $|\psi\rangle$:

$$\hat{\rho}_A = \mathrm{Tr}_{\bar{A}} \left|\psi\right\rangle \left\langle\psi\right| \tag{5.22}$$

then we eliminate the unitary operations by the beam splitter that acts only on A because the entanglement entropy is not sensitive to such unitary operation:

$$S'_A = \mathrm{Tr}\, \hat{U}\hat{\rho}_A\hat{U}^\dagger \ln \hat{U}\hat{\rho}_A\hat{U}^\dagger = \mathrm{Tr}\, \hat{\rho}_A \ln \hat{\rho}_A \tag{5.23}$$

After the reduction, we obtain the tensor network in fig. 5.8. There are two key observations to make: if each leg contributes to the entanglement entropy, then the system does not follow the area law; and in fact, the entanglement structure is the same as the entanglement structure of flat space-time!

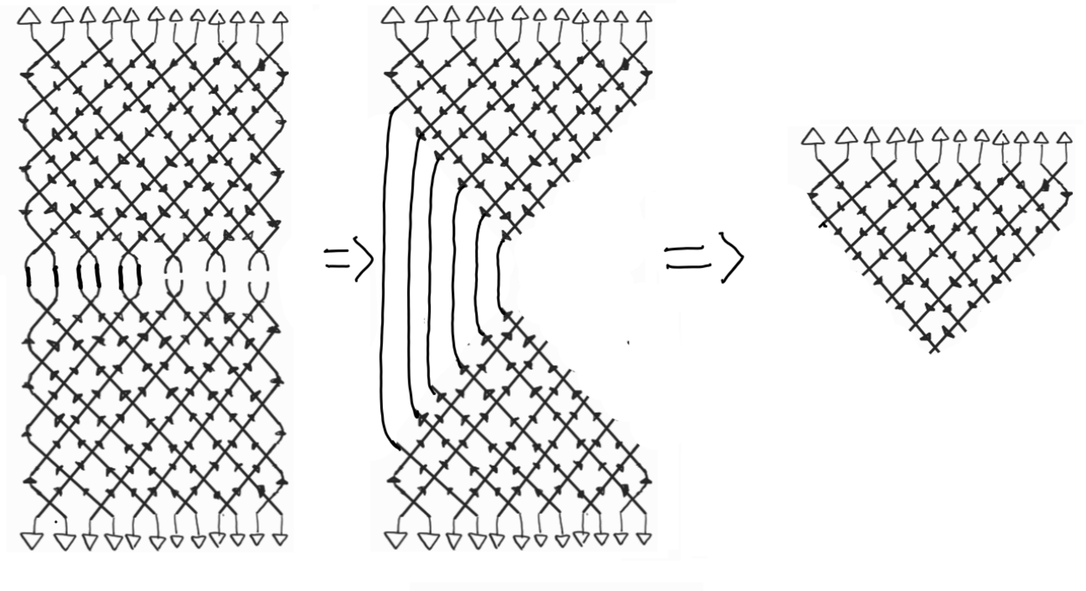

Figure 5.8: The diagram on the left represents the density matrix of an subsystem size $L = 6$ (characterised by its 6 outputs) of the boson sampling tensor network of size $L = 12$. The top triangles are the 12 initial input states, and we trace over the left subsystem to obtain the density matrix. In the middle, we perform operation in eqn. 5.23 to eliminate the unitary evolution that contributes only to the right subsystem. Finally, we isolate the part of the TN that contributes to the bipartite entanglement entropy.

From the first key observation, we can immediately derive the analytical upper bound. Suppose we send in $N - 1$ photons to the boson sampling device, then the max occupancy for each output is $N - 1$. Each leg in the TN can then maximally contribute to $\ln N$ entanglement entropy if the state is random because the maximal occupancy is N. For a large enough system, we expect that every leg shares the same entanglement entropy at equilibrium due to the translational symmetry of the boson sampling device. Applying the triangular inequality argument $\sum_a S_a \geq \sum_a E_a \geq E$, where S_a are the individual upper bounds and E is the entanglement entropy of the subsystem, then we obtain:

$$E(A) = E(\bar{A}) = \min\left(L_A, L_{\bar{A}}\right) \ln N \tag{5.24}$$

This is explicitly a volume law - the entanglement entropy is explicitly proportional to the system size. This analysis is consistent With Page's calculation, except the general upper bound for a random pure state has a first order correction[44]:

$$E(A) = \ln \mathcal{D}_A - \frac{1}{2}\frac{\mathcal{D}_A^2}{\mathcal{D}} \tag{5.25}$$

where $\mathcal{D}_A$ is the Hilbert space dimension for system A.

However, there is multiple problems with this estimation. Firstly, this is not a tight upper bound, and the upper bound changes depending on the parameter. Secondly, it is not true that boson sampling devices always follow a volume law.

Back to the TN representation, the region of unitary operators that we eliminated is analogous to the Rindler wedge to the subregion of a flat space-time[45]. It is know that any perturbations to the Hamiltonian within the Rindler wedge will not affect the entanglement entropy of the subregion, and this is consistent to our analysis. This is not surprising, because the boson sampling device has a partial order structure, but the parallel is interesting and might shed light to the studies of space-time entanglement entropy.

5.4.3 Entanglement Spectrum for Low Transmission Coefficient with non-linear Interaction Term

Although the entanglement spectrum in eqn. 5.24 is not tight, we can improve the argument via replacing it with a more suitable entanglement contribution for each leg. Suppose we tune the transmission coefficient of the beam-splitter to low, and add some form of coupling between photons; then the time it takes for a photon to travel to other sites is very large when the photon travels down the sampling device. In this limit, the photon does not scramble like a random state, so each leg is an open system that interacts slowly to the environment. The entanglement entropy of the leg is maximised in the Gibbs state, so instead we would expect the volume to be:

$$S(L_A) = \min\left(L_A, L_{\bar{A}}\right)\left[(1+\bar{n})\ln(1+\bar{n}) - (\bar{n})\ln(\bar{n})\right] \tag{5.26}$$

Although this sounds like a hand wavy argument, we can make a rigorous derivation of it!

First, we observe that for large transmission coefficient, the beam splitter parameter θ is small. Let us define $\theta = \delta t z$, then in each time-step the operator becomes $e^{-iz(\hat{a}^\dagger\hat{b}-\hat{b}^\dagger\hat{a})i\delta t}$, this is equivalent to the Suzuki-Trotter approximation for the Hamiltonian for nearest neighbour free boson hopping:

$$\hat{H}_{\text{free}} = \sum_i -iz(\hat{a}_i^\dagger\hat{a}_{i+1} + h.c.) \tag{5.27}$$

In fact, this Hamiltonian still describes the scrambling of particles in a box as a quadratic Hamiltonian[46], just that the process is slower, because there is no interactions between particles. Thus, for the system to thermalise we need to add an interaction term:

$$\hat{H} = \sum_i -iz(\hat{a}_i^\dagger\hat{a}_{i+1} + h.c.) + \lambda\sum_i(\hat{a}_i^\dagger\hat{a}_i\hat{a}_{i+1}^\dagger\hat{a}_{i+1} + h.c.) \tag{5.28}$$

This is known as the quantum chaotic Hamiltonian. For such Hamiltonian, the state thermalises as the random canonical state[47][5]. The random canonical state is not the eigenstate of the system. It fluctuates but it remains stable. For a closed system of size L, and N bosons, the state is defined as:

$$|\psi_N\rangle = \frac{1}{\sqrt{D}}\sum_i z_i\,|i\rangle \tag{5.29}$$

where $|i\rangle$ is the set of all possible configuration $|n_1, ..., n_L\rangle$ and z_i is a normally distributed real random number with 0 mean and 1 variance such that $\sum_i z_i^2 \to D$ for large system size. Meanwhile, D is the dimension of the Hilbert space $\binom{N+L-1}{N}$ (just combinatorics of how many ways to put N balls of the same colour into L boxes). This state is thermalised because no configuration is preferred, and the utility of the normal distribution will be clear later.

Next we want to split the state into subsystems of size L_A and $L - L_A$, such that the bipartite eigenstate can be rewritten as:

$$|\psi_N\rangle = \sum_{N_A=0}^{N} \sum_{j=1}^{D_{N_A}} \sum_{k=1}^{D_{N-N_A}} \frac{z_{j,k}(N_A)}{\sqrt{D}} |j, N_A\rangle |k, N - N_A\rangle \tag{5.30}$$

where $D_{N_A} = \binom{N_A+L_A-1}{N_A}$ and $D_{N-N_A} = \binom{N-N_A+L-L_A-1}{N-N_A}$, representing the total number of states in the subsystem, and j, k represents the configurations of the subsystem. We can check that summing up the number of configuration in the subsystems gives the right amount of total configurations[1]:

$$\sum_{N_A=0}^{N} \binom{N_A + L_A - 1}{N_A} \binom{N - N_A + L - L_A - 1}{N - N_A} = \binom{N + L - 1}{N} \tag{5.31}$$

$$\sum_{N_A=0}^{N} \frac{\binom{N_A+L_A-1}{N_A}\binom{N-N_A+L-L_A-1}{N-N_A}}{\binom{N+L-1}{N}} = 1 \tag{5.32}$$

Terms in eqn. 5.32 forms a probability distribution that will be the key to the derivation.

From $\hat{\rho}_A = \mathrm{Tr}_{\bar{A}} |\psi_N\rangle \langle\psi_N|$:

$$\hat{\rho}_A = \sum_{N_A=0}^{N} \sum_{j,l=1}^{D_{N_A}} \frac{M(j, l, N_A)}{D} |j, N_A\rangle \langle k, N_A| \tag{5.33}$$

where,

$$M(j, l, N_A) = \sum_{k=1}^{D_{N-N_A}} z_{j,k}(N_A) z_{l,k}(N_A) \tag{5.34}$$

The random number $z_{j,k}(N_A)$ fluctuates so we want to find a mean field description to the density matrix:

$$\langle M\rangle = \sum_{k=1}^{D_{N-N_A}} \langle z_{j,k}(N_A) z_{l,k}(N_A)\rangle \tag{5.35}$$

when $j \neq l$, we know that the two random numbers have no correlation:

$$\langle M\rangle = \sum_{k=1}^{D_{N-N_A}} \langle z_{j,k}(N_A)\rangle \langle z_{l,k}(N_A)\rangle = 0 \tag{5.36}$$

---

[1] This relation can be immediately derived from expanding $\frac{1}{(1+x)^a} \frac{1}{(1+x)^b} = \frac{1}{(1+x)^{a+b}}$

when $j = l$, the variances average to D_{N-N_A}, so the average reads:

$$\langle M \rangle = D_{N-N_A} \delta_{jl} \tag{5.37}$$

and thus the average density matrix:

$$\bar{\hat{\rho}}_A = \sum_{N_A=0}^{N} \sum_{j=1}^{D_{N_A}} \frac{D_{N-N_A}}{D} |j, N_A\rangle \langle j, N_A| \tag{5.38}$$

Now we see that the idea of getting a normal distribution is to diagonalise the mean density matrix, so the derivation is actually not dependent on the normal distribution. Its Von-Neumann entropy reads:

$$\begin{aligned} \bar{S}(L_A) &= -\sum_{N_A=0}^{N} \frac{D_{N_A} D_{N-N_A}}{D} \ln \frac{D_{N-N_A}}{D} \\ &= -\sum_{N_A=0}^{N} \frac{D_{N_A} D_{N-N_A}}{D} \ln D_{N-N_A} + \ln D \end{aligned} \tag{5.39}$$

For the sake of simplicity in the derivation, we define $N_B = N - N_A$. Using Stirling's approximation:

$$\begin{aligned} \ln \binom{N+L-1}{N} &= (N+L-1)\ln(N+L-1) - N\ln N - (L-1)\ln(L-1) \\ &= (L-1)\left((1+n)\ln(1+n) - n\ln n\right) \end{aligned} \tag{5.40}$$

where $n = \frac{N}{L-1}$, so $\ln D_{N_B} = (L_B - 1)((1+n_B)\ln(1+n_B) - n\ln n_B)$, $n_B = \frac{N_B}{L-1}$.

For simplification, we take the log of the probability:

$$\begin{aligned} \ln \frac{D_{N_A} D_{N-N_A}}{D} = &(L_A - 1)((1+n_A)\ln(1+n_A) - n_A \ln n_A) + (L_B - 1)((1+n_B)\ln(1+n_B) - n_B \ln n_B) \\ &- (L-1)((1+n)\ln(1+n) - n\ln n) \end{aligned} \tag{5.41}$$

expand the term around $n_A = n + \delta n_A$ and $n_B = n + \delta n_B$ to the second order, then we find out that the zeroth and first order term vanishes, and the second order reads:

$$\ln \frac{D_{N_A} D_{N-N_A}}{D} = -\frac{L_A \delta n_A^2}{2n(n+1)(1-f)} + \mathcal{O}(\delta n_A^3) \tag{5.42}$$

where $f = L_A/L$. The bad news is that the range of δn_A is greater than 1, so the higher order terms matter and we cannot approximate the distribution as a Gaussian distribution, but the good news is nonetheless the 0th order of the entanglement entropy is distribution independent. The idea of this expansion is such that we can write the distribution as a function of δn_A. Next, we expand $\ln D_{N_B}$ to get:

$$\ln D_{N_B} = (L_B - 1)((1+n)\ln(1+n) - n \ln n) + \mathcal{O}(\delta n_A) \tag{5.43}$$

From eqn. 5.39, we get:

$$\begin{aligned} &- \sum_{N_A=0}^{N} \frac{D_{N_A} D_{N-N_A}}{D} ((L_B - 1)((1+n)\ln(1+n) - n\ln n) + \mathcal{O}(\delta n_A)) + \ln D \\ &= L_A((1+n)\ln(1+n) - n\ln n) - \sum_{N_A=0}^{N} P(\delta n)\mathcal{O}(\delta n_A) \end{aligned} \tag{5.44}$$

It turns out that the contribution of the last term is of order $\mathcal{O}(1)$[2]. Thus, we have derived the volume law for high transmission coefficient. This derivation verifies our intuition that each leg in the boson sampling tensor network contributes $(1+n)\ln(1+n) - n\ln n$ entropy to the subsystem.

---

[2] We can check this by approximating the distribution as Gaussian, and the dimension of the actual distribution should be consistent with this approximation.

Chapter 6

Simulation Results

6.1 Single Fibre Loops

Results of the single fibre loops are already available in [37]. The first part of this project is to reproduce the simulation results of the paper, and then we pursue the generalisation.

6.1.1 Simulation Method

Since the future states of the single fibre loop do not contribute to the entanglement entropy, we only need to perform the QR decomposition of the input state and the beam splitter to determine the singular values, as explained in fig. 5.7. From the singular values, we can calculate the density matrix of the single fibre loop state useful for determining the key physical properties.

6.1.2 Sanity Check

Sanity can be checked via computing some physical quantities of the MPS. Denote the transmission coefficient as τ. In the set-up, we send one photon into the single fibre loop at each iteration. Thus, the expected photon number of the first output photon should be the same as τ. At equilibrium, the output photon number should be equal to the input photon number, which is 1. The result of this check is shown in fig. 6.1, and indeed the two key requirements satisfy conditions.

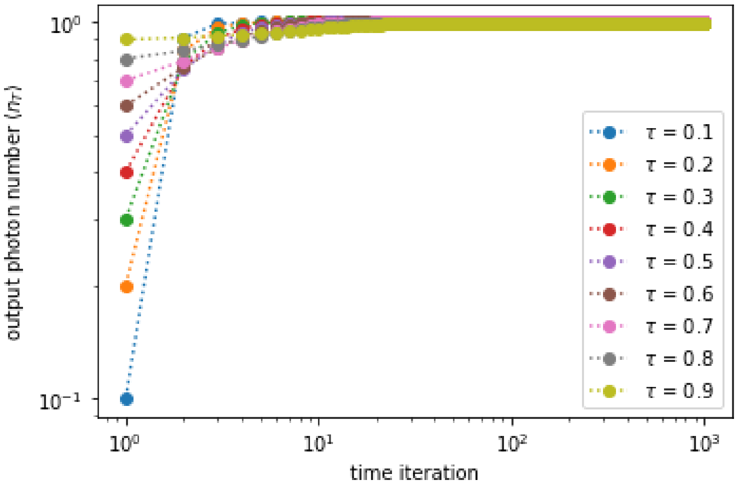

Figure 6.1: This diagram shows the expected photon number of the output time-bin mode in log-log scale. We can see that the initial photon number matches τ, and the final output photon number reaches the universal equilibrium – $\langle n \rangle = 1$

We can also check whether the photon numbers are conserved at each iteration via calculating the loop state photon numbers, and the result is available in fig. 6.2. The last observation to make for sanity is that it takes a long time loop state to saturate at $\tau = 0.9$ compared to

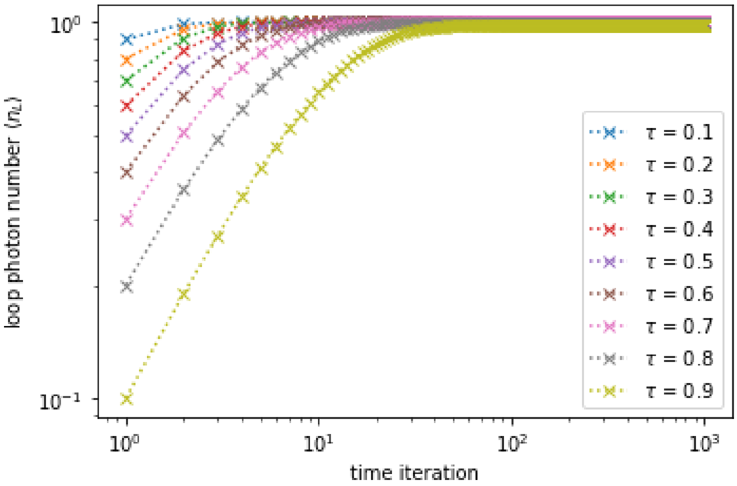

Figure 6.2: This diagram shows the expected photon numbers of the loop mode in log-log scale. We see that the initial loop mode photon is instead proportional to the reflection coefficient. Thus, the conservation of photon number is satisfied. Meanwhile, the final loop photon number too reaches the universal equilibrium – $\langle n \rangle = 1$.

$\tau = 0.1$. That makes sense because it is hard for photons to access the loop at high τ.

6.1.3 Entanglement Entropy

Two plots are made to demonstrate that the entanglement entropy reaches an upper bound, and follows the derived analytic upper bound. First, we calculate the evolution of the entanglement entropy of the loop state concerning time. In this set-up, we send in one photon for each iteration. However, the real test is whether the analytic upper bound describes the maximal entanglement entropy. In the simulation, we find that the maximal entanglement entropy with respect to different photon numbers follows tightly the analytic upper bound.

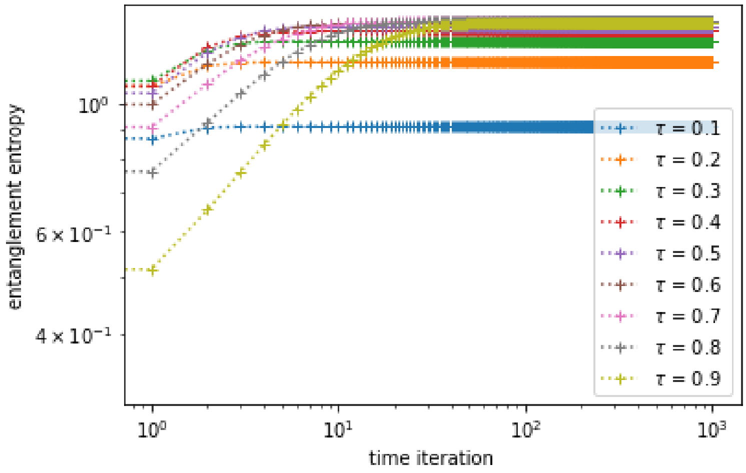

Figure 6.3: This diagram shows the loop entanglement entropy between the loop state and the past output time-bin mode. All entanglement entropies saturate at a maximum value for all tested transmission coefficients, demonstrating the area law of single fibre loop.

Analytic	Simulation
1.3868717842365972	1.386512879321367
1.9181253049039542	1.9178516933470275
2.2664651916898104	2.2659406460250415
2.5121624989883813	2.510263087446124

Table 6.1: It is not clear in this plot whether the maximal entropy is bounded from above, so a table is made to compare the bound and the entropy for $\langle n \rangle = 1, 2, 3, 4$.

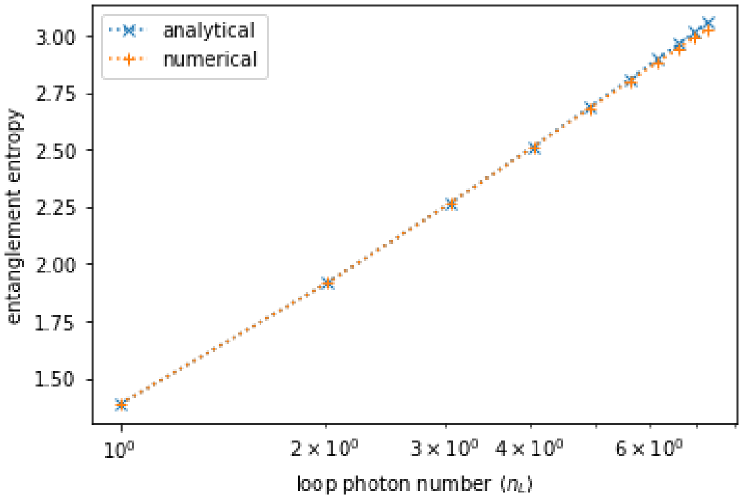

Figure 6.4: This diagram shows the analytic upper bound and the maximal entanglement entropy concerning the average photon number in the loop mode. We see that the bound is tight, meaning that the prediction is correct. This plot also informs us that the entanglement entropy scales logarithmically with the number of input photon. A slight deviation appears between the bound and the max entropy at high $\langle n_L \rangle$ because the bond dimension is fixed at $nl = 30$ for increasing expected loop photon number in this plot.

6.1.4 Implication of the Area Law for Simulation

Through the two plots, we can confirm that the single fibre loop follows the area law. That is, the loop state entanglement entropy is bounded from above. Computationally, that would also mean that we can truncate the bond dimension in the MPS representation as an approximation. However, to obtain a good approximation in this simulation: with an error within 0.1% of the real value, the minimal bond dimension is required to be multiple times higher. For example, the bond dimension for simulating one input photon per iteration is chosen to be $nl = 10$ for the error to be within 0.01%. Imagine now we simulate instead a two fibre loop set-up. The bond dimension to the same error rate would be $nl = 100$ because the number of loop states doubles – the bond dimension scales exponentially with the number of loops! That would also correspond to an exponential increase in computational cost as we scale up the number of fibre loops linearly.

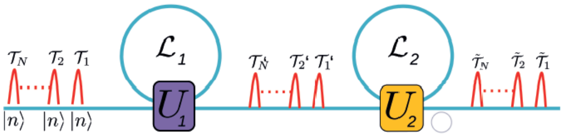
$\mathcal{T}_N$
$\mathcal{T}_2$
$\mathcal{T}_1$
$|n\rangle$
$|n\rangle$
$|n\rangle$
$\mathcal{L}_1$
U_1
$\mathcal{T}_N'$
$\mathcal{T}_2'$
$\mathcal{T}_1'$
$\mathcal{L}_2$
U_2
$\tilde{\mathcal{T}}_N$
$\tilde{\mathcal{T}}_2$
$\tilde{\mathcal{T}}_1$

Figure 6.5: This diagram shows the optical set-up of two fibre loops in sequence. The TN representation is available in the appendix.

6.2 Two Fibre Loops

Results in [37] did not demonstrate that any fibre loops architecture follows the area law. Thus, the second part of the project is to essential show that through simulations. There are two types of fibre loops set-up: loops in sequence and loop in loop architecture, as shown in fig. 6.5 and 6.6. Naively, we would expect that the loop in loop architecture to be more complex because the two loops can interact bilaterally; while for loop in sequence, one loop is in strict causal order to the other loop.

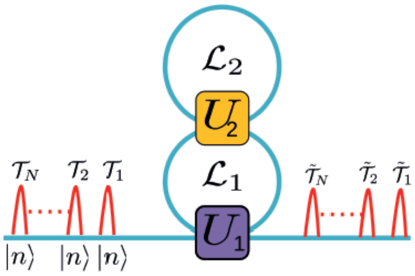
$\mathcal{L}_2$
U_2
$\mathcal{L}_1$
U_1
$\mathcal{T}_N$
$\mathcal{T}_2$
$\mathcal{T}_1$
$|n\rangle$
$|n\rangle$
$|n\rangle$
$\tilde{\mathcal{T}}_N$
$\tilde{\mathcal{T}}_2$
$\tilde{\mathcal{T}}_1$

Figure 6.6: This diagram shows the optical set-up of two fibre loops with one within the other. The TN representation is available in the appendix.

6.2.1 Loops in Sequence

We first calculate the time evolution of the expected photon number in the second loop states. The expected photon number in the first loop is the same as the fig. 6.2, but the second loop photon number demonstrates an interesting behavior, as shown in fig. 6.7. Such interesting behavior again informs us that the simulation is functioning properly.

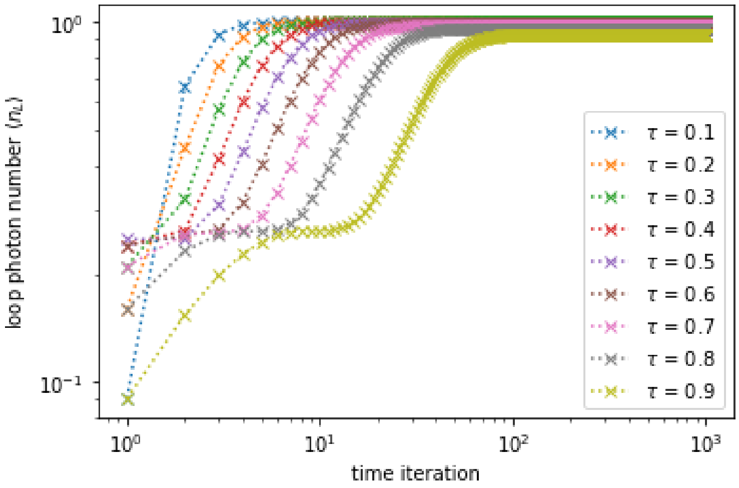

Figure 6.7: This diagram shows the photon number of the second loop state. We see that there is two equilibrium in the second loop state. The first equilibrium appears when the second loop state saturates before the first loop does. When the first loop is saturated, however, more photons are available for the second loop state such that the second loop state rises to its final equilibrium.

6.2.2 Two Sequential Loops Entanglement Entropy

Analysis of the entanglement entropy for two sequential loops is exactly the same as the one loop entanglement analysis, and the results are shown in fig. 6.8 and 6.9.

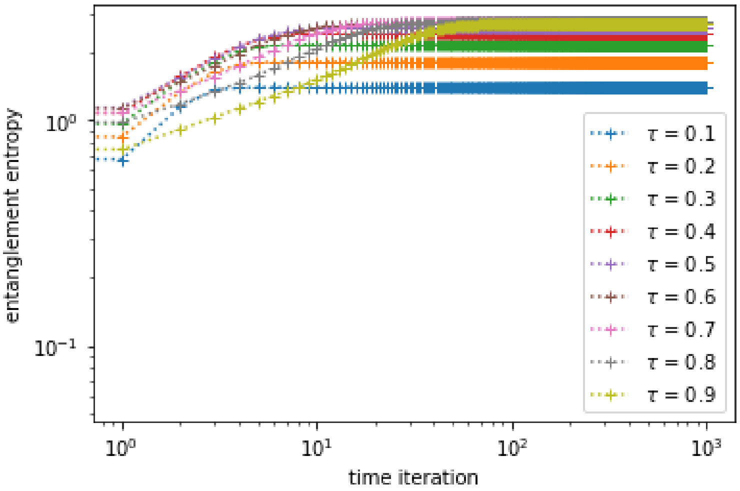

Figure 6.8: This diagram shows the two sequential loops entanglement entropy time evolution. Again, all entanglement entropy saturate despite of the transmission coefficient.

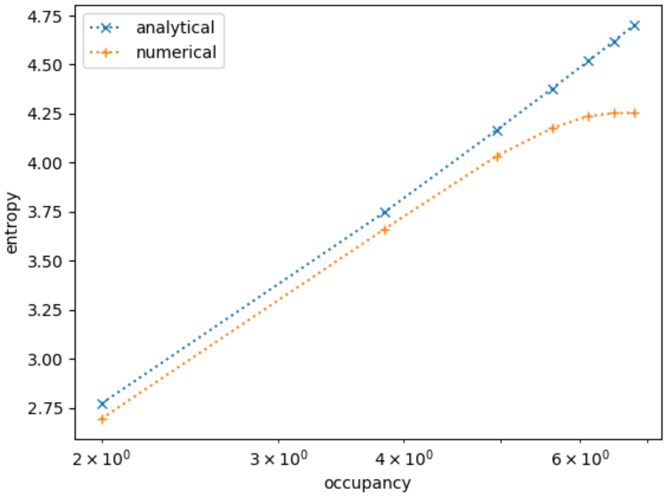

The plot suggests that two sequential fibre loops satisfy the area law, and the analytical upper does it job as well, except the entanglement entropy is strictly bounded from above.

Figure 6.9: This diagram shows the analytic upper bound vs. max numerical entanglement entropy for two loops in series. It is much clearer this time that the numerical upper bound is systematically lower than the analytical upper bound for all photon numbers. Again the deviation for large photon number at the RHS of the plot is due to a non-sufficiently large enough bond dimension.

6.2.3 Non-sequential Two Fibre Loop

Now we study the loops state properties of the loop in loop set-up, starting with the expected photon numbers in the two loops shown in fig. 6.11 and 6.12.

Besides the interesting oscillatory effect of the photon numbers in the loop, the rest of the properties are similar to the two sequential loop set-up – the time to saturation and the saturated photon number. That is not surprising because these are the universal properties of fibre loops.

6.2.4 Loop in Loop Entanglement Entropy

The result shows that the two loops arrangement follows the area law in the two plots. Through the two plots, we see that it is harder for the two-loop set-up to reach the equilibrium; its maximal entanglement entropy appears to be higher than the loops in sequence across all τ. Meanwhile, the maximal entropy w.r.t. the transmission coefficient is closer to each other compared to the loop in sequence entropy, meaning that the entropy in this set-up is more

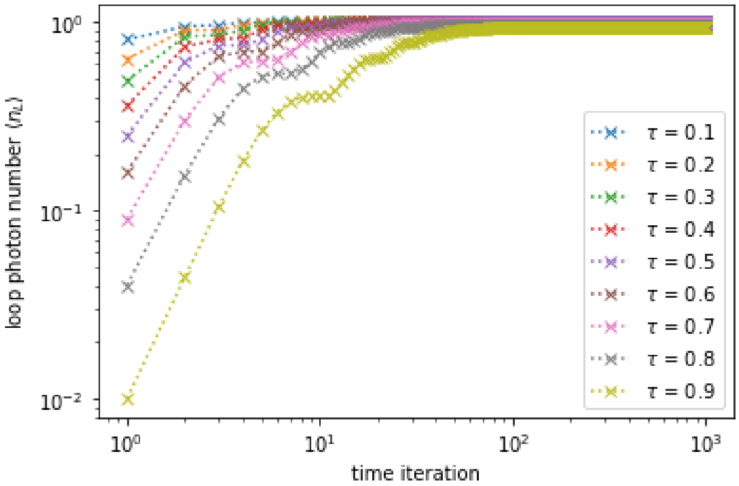

Figure 6.10: This diagram shows the expected photon number of the first loop state. Except for the case of low transmission coefficient, the photon number in the first loop increases in an interesting zigzag manner. That is because the photon number appears to oscillate between the first and the second loop.

convergent to the analytic upper bound. Looking at the plot for the analytic upper bound, it suggests that indeed the upper bound this time is tight if we ignore the truncation error from the bond dimension.

These results suggest two things: the loop in loop set-up leads to a slightly more complex dynamics in the loops than the loops in sequence set-up. That agrees with our intuition pointed out in the beginning that is because the second loop in sequence does not interact with the first loop in sequence in the sequential set-up. Nonetheless, both set-up are bounded by the analytic upper bound in eqn. 5.19. In the simulation, $nl = 10$ is used for a single loop state, so the two loop state dimension in total reads $nl^2 = 100$. For the physical leg, $nt = 10$ is used because the output photon occupancy is at most $\langle n \rangle = 1$ per interation.

6.2.5 Discussion – Complexity for Fibre Loops

The three examples of fibre loops confirm that the entanglement entropy follows the analytic upper bound. Simulation for three loops or above is not made simply because, following the convention we use for the simulation, the total loop state will have dimension $nl^3 = 1000$, meaning that it will take a few hours to simulate the entanglement entropy for a three-loop

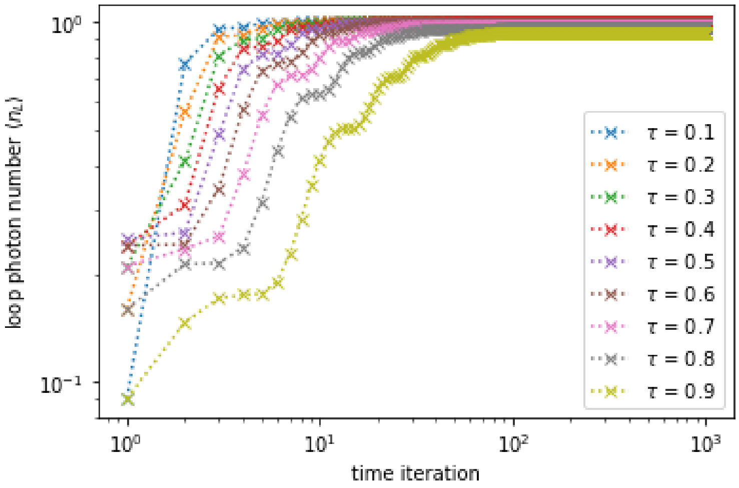

Figure 6.11: This diagram shows the expected photon number of the second loop state. Notice that the oscillation that is complementary to the first loop state.

set-up in a computer.

Again, this is reflected directly in the MPS analytic upper bound. From the equation, the entanglement entropy for n loops with one photon input per iteration is $n \ln 4$. Integer growth of the entanglement entropy would imply an exponential growth of the computational cost. For example, it takes around 40 seconds to make the entanglement entropy vs. max numerical entropy graph for one loop; for three loops, that would be $\sim$ 18 hours!!

While the proof that fibre loops follow the area law is valid, there are two difficulties we face when performing the simluation.

- Entanglement entropy still scales up linearly with the number of loops
- The unbounded quantum number for photon implies that the bond dimension must be comparably higher than the expected quantum number for a good approximation

Thus, the area law does not guarantee the quantum system to be classically easy to simulate. It places a limit on the complexity of the system, but we have shown that the complexity may be so high that we cannot reach the limit in the first place, as in the three fibre loop case. Thus, for many fibre loop set-up, a quantum simulator still demonstrates quantum supremacy.

The situation improves if the quantum number is bounded from above. For example, if we

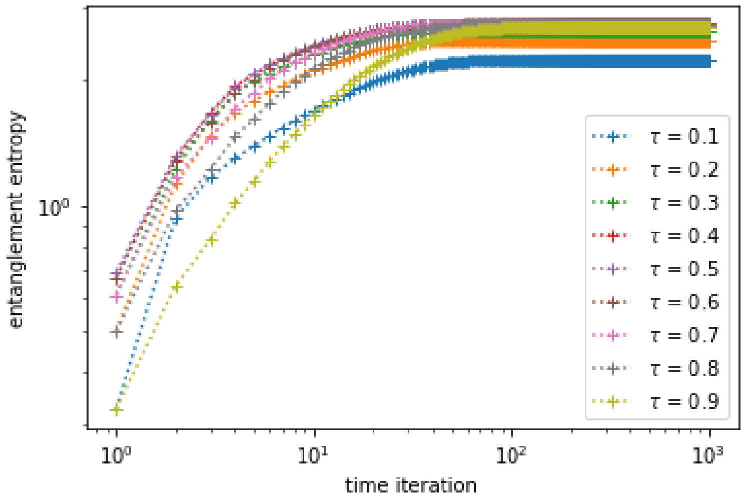

Figure 6.12: This diagram shows the loop in loop entanglement entropy time evolution. All entropy saturate as before despite the transmission coefficient. What is perhaps more unique is the transient state. At $\tau = 0.1$, it takes a much longer time $\sim 10^2$ for the loop and loop set-up up to saturate compared to the loops in sequence $\sim 4 \times 10^0$. This suggests that the loop in loop set-up produces more complex dynamics in the loop states.

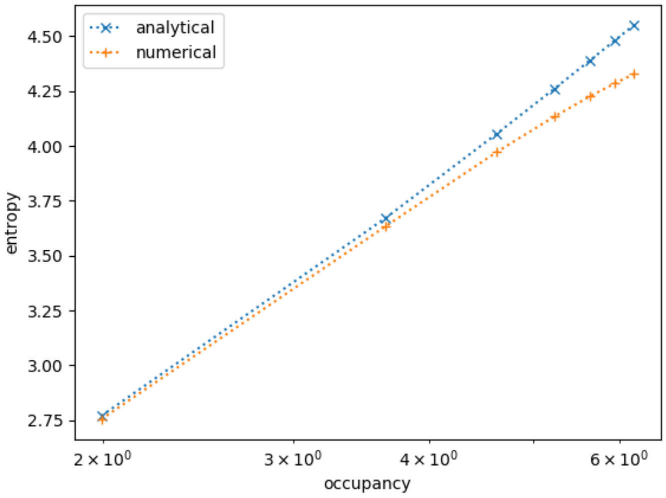

Figure 6.13: This diagram shows the analytic Upper bound vs. max numerical entanglement entropy for the loop in loop set-up. Compared to the two loops in sequence, the analytic upper bound is rather tight compared to the numerical result, and this again suggests more complex dynamics in the loop in loop set-up.

perform the same simulation for fermions, three loops will only have a bond dimension of $nl^3 = 8$ because every loop state at most has dimension $nl = 2$. The area law would be a stronger condition compared to the boson case, and a classical computer is more tolerant to the number of fibre loops in the context of multi-fibre loops.

Nonetheless, if the complexity is within reach, then the area law guarantees that the system of interest has computational cost that is polynomially sensitive to the growth to the system size. In our study, we simulate the entanglement entropy until the system size reach 10^3 (system size is proportional to the iteration), because the computational cost always grows linearly to the system size in the one-dimensional area law set-up. In that sense, area-law system undermines quantum supremacy.

6.3 Boson Sampling

Since the computational limit for many fibre loops set-up is already well-understood through this dissertation, we turn our attention to the non-area law bosonic circuit to study its entanglement entropy type and to understand in which context the non-area law leads to quantum supremacy for the NISQ era.

6.3.1 Simulation Method

Simulation of parallel bosonic circuit is different the fibre loops simulation. In the set-up, we feed in all input states of the boson sampling device with one photon $|1\rangle$, and runs the TEBD method to descibe the situation when the photons travel down the beam splitters.

6.3.2 Sanity Check

There are two properties to check before running the simulation – normalisation and expected output photon numbers. Since the operators are all unitary, the normalisation of the final state should still be 1. In the simulation, there are two reasons why the normalisation fails to be 1 – either the unitary operator is not unitary because of bugs in the program, or the occupancy is not high enough to contain all information of the system. Note that the beam splitter operator has an unbounded occupancy as shown in eqn. 5.3. However, the maximal number of dimension needed for the simulation is just the maximal possible occupancy, which is the total number of photons in the input.

Checking the expected number of output photon is useful because it checks whether the canonical form is functioning properly. As mention in fig. 3.3, the information needed to compute the correlator should only be limited to the local site and singular value in the canonical form. After checking the unitarity and canonical form, we are ready to make some simulations.

6.3.3 Low Transmission Coefficient with Cross Kerr Interaction

Back to the derivation of the volume law for boson sampling with High transmission coefficient and some interaction term. With the Trotter-Suzuki approximation, the interaction term can be model as the cross-Kerr operator, defined as $\exp(-i\lambda\hat{a}_i^\dagger\hat{a}_i\hat{a}_{i+1}^\dagger\hat{a}_{i+1})$. The expression we derived is in fact used to model a non-linear sampling device when the parameter τ and λ are small. Next we can compare the analytic upper bound to the entanglement entropy shown in fig. 6.14.

While the analytic upper bound is a success, when we remove the interaction, instead we obtain the following result in fig. 6.15.

6.3.4 Free Bosons

Since the free boson system does not thermalise, the Gibbs state argument for the volume law fails. While being confused at what curve describes the entanglement entropy, there are three properties to study about the entanglement entropy. First, if we plot the Hilbert space dimension of the singular value across the sampling device, we obtain a Gaussian distribution

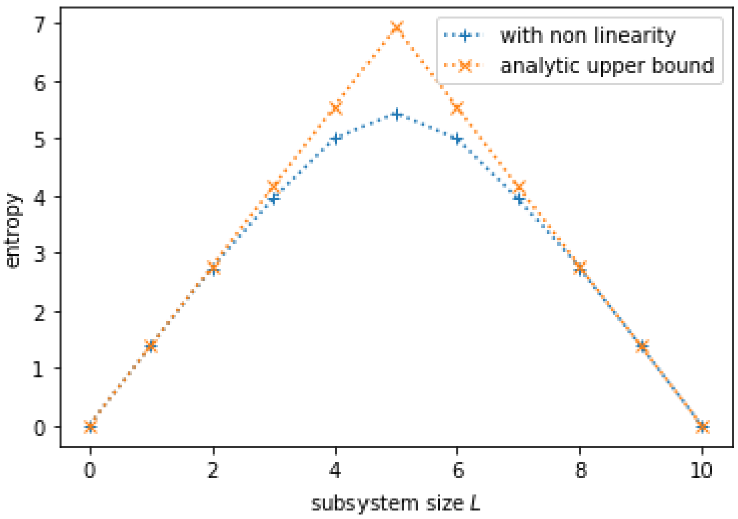

Figure 6.14: Entanglement entropy of non-linear sampling device vs. the analytic upper bound. The sampling device is run over 50 layers with system size $L = 10$ such that the system reaches an equilibrium. The result confirms that the upper bound is indeed the right description for non-linear sampling devices. Entanglement entropy of this type is an example of Page curve, funny enough[5].

given by fig. 6.16. Second, the distribution of individual singular values is all nearly flat, given by fig. 6.17. Finally, the distribution is in fact insensitive to the transmission parameter, given by fig. 6.18. The third point implies that the entanglement entropy is universal despite the transmission coefficient.

6.3.5 Classical Simulatability of Boson Sampling Device

The first and second observation directly implies that the analytic upper bound is expected to be parabolic. If the distribution of the singular value is flat, the density matrix is a multiple of the identity, meaning that the corresponding Von-Neumann entropy is the log of the Hilbert space size. Meanwhile, the log plot shows that the space is a parabola, thus the parabolic analytic upper bound. The third observation implies that if an analytic upper bound is derived, it is universal for the boson sampling device regardless of the transmission coefficient.

We can make an estimated analytic upper bound for the boson sampling device with the above information, we would expect that the upper bound takes the form $S = C\left(L_A - \frac{L_A^2}{L}\right)$ simply because the entanglement entropy must be 0 at the boundaries of the boson sampling device

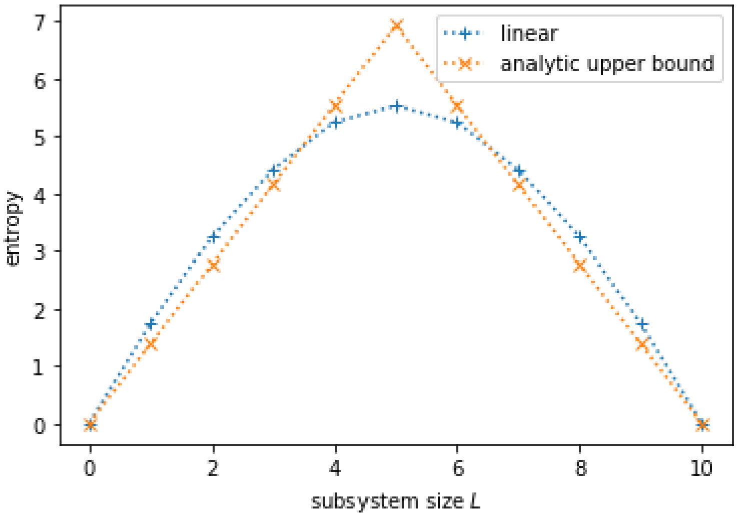

Figure 6.15: Without the interaction term, photons within the sampling device interact linearly as superposition, so thermalisation does not take place. Instead, we need another description of the entanglement entropy.

(the bipartition cut the system into a subsystem of size $L_A = L$ and $L_{\bar{A}} = 0$). To find out the constant C, we observe that the edge entanglement entropy approaches the entanglement entropy given by eqn. 5.25 for a random pure state that is insensitive to the finite size effect. Near the edge, the entanglement entropy approaches:

$$S(A)_{L_A \to 0} = L_A \ln N \tag{6.1}$$

where N is the maximal occupancy equal to the total photon number in the device plus one. Thus, for small L_A, we find $C = \ln N$. The estimation is plotted against the predicted entanglement entropy from eqn. 5.25, the simulation and a numerical estimate of the entanglement entropy based on the virtual bond Hilbert space size in fig. 6.19.

Thus, the estimated upper bound describes the numerical result with some systematic error. In fact, this success is not coincident. We can rewrite the upper bound in the form:

$$\ln N \left(L_A - \frac{L_A^2}{L} \right) = \ln N^{L_A} - \frac{(\ln N^{L_A})^2}{\ln N^L} = \ln D_A - \frac{(\ln D_A)^2}{\ln D} \tag{6.2}$$

where D_A and D are respectively the Hilbert space dimension of subsystem A and the system. The bound is known as the *first order universal upper bound*. It has been shown that such

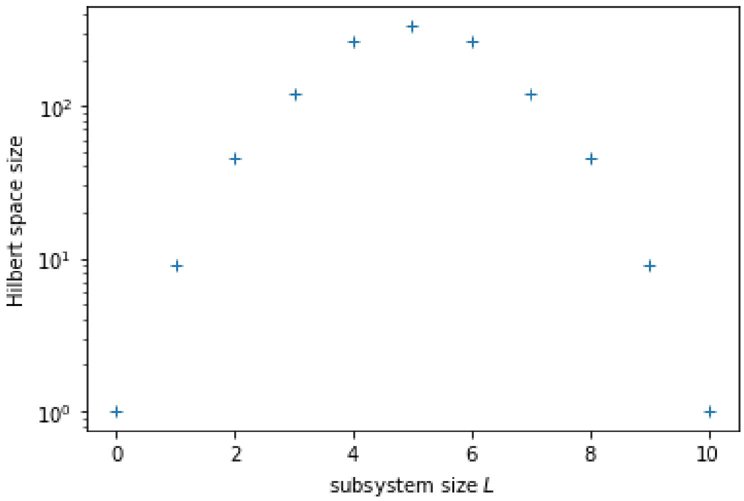

Figure 6.16: This diagram shows the Hilbert space distribution across the boson sampling device. The numerical result shows that the distribution is parabolic in the log plot.

bound describes the analytic bound for many bodies quadratic fermionic Hamiltonian[46]. In this dissertation, we numerically show that the analytic bound also works for the bosonic case. Unfortunately, however, the exact derivation of the first order bound is not yet found for boson.

6.3.6 Discussion of Boson Sampling Entanglement Entropy

We numerically studied two types of analytic upper bound for the boson sampling devices – non-linear sampling included the cross-Kerr interaction and linear boson sampling. We find out that a non-linear sampling device with uniform beam-splitter and cross-Kerr operators with small parameters produces an entanglement entropy that follows the volume law $L_A((1+\bar{n})\ln(1+\bar{n})-\bar{n}\ln\bar{n})$. This expression is universal and is independent of the system size L.

For a general boson sampling device without non-linearity, the entanglement entropy follows a quadratic law in L_A, to the first order. To see how the entropy scales with the system size L, we fix the ratio $f=\frac{L_A}{L}$, then the quadratic expression becomes $Lf(1-f)\ln N$. In this form, the entanglement entropy scales linearly with L as we increase the system size.

Meanwhile, what is rather interesting in both scenarios is that the entanglement entropy does not scale linearly with the particle numbers, but instead as logarithmic. To see how it is true for the for the non-linearly sampling device: for large $\bar{n}$, $(1+\bar{n})\ln(1+\bar{n})-\bar{n}\ln\bar{n} \to \ln\bar{n}$.

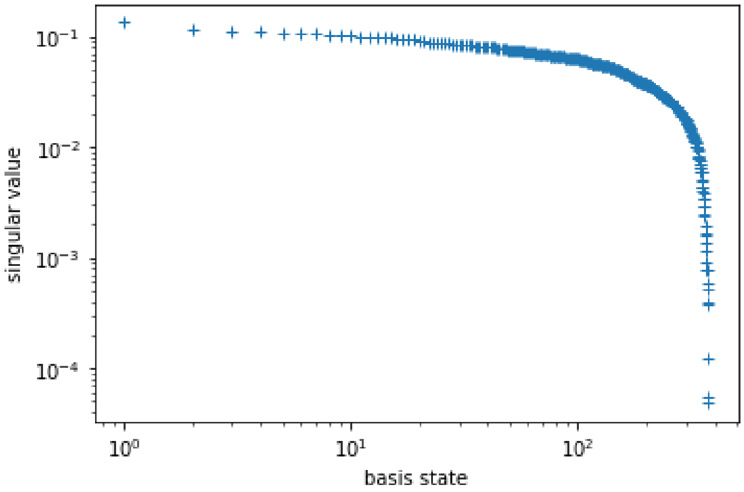

Figure 6.17: This diagram shows the singular value of an example bipartition at $L = 5$. The distribution is almost flat, meaning that the system resembles a random pure state rather than a thermal state. Computationally speaking, a truncation to the bond dimension (that holds the singular value) in this case would be harmful to the simulation.

Roughly, speaking, increases of particle numbers in the boson sampling device then scale up the computational polynomially. Although it is classically hard to simulate a boson sampling device as we scale up the system size, it is classically tractable to simulate boson sampling while increasing the particle numbers.

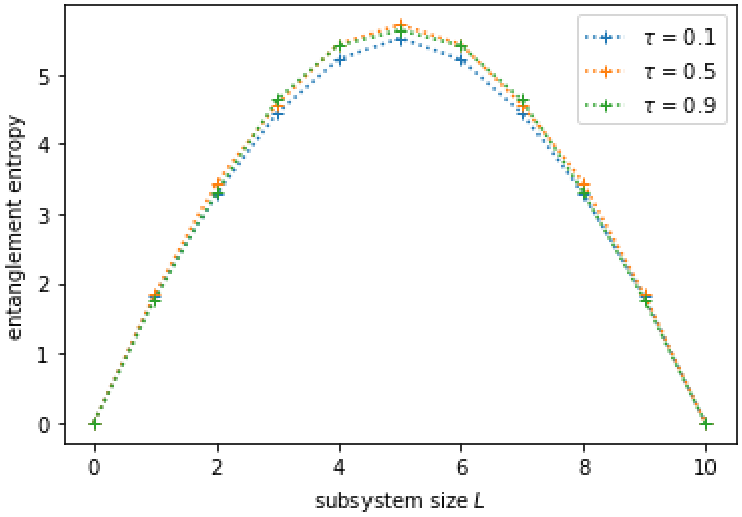

Figure 6.18: Despite of the transmission coefficient τ, the entanglement entropy spectrum of the boson sampling device in equilibrium remains the same. It implies that one only needs to derive one universal upper bound to characterise the boson sampling entanglement entropy spectrum.

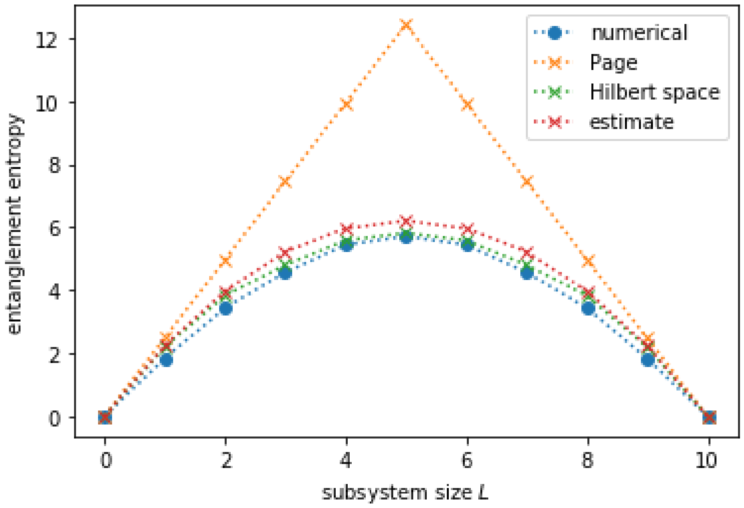

Figure 6.19: The estimate upper bound for system size $L = 10$ is compared to the analytic upper bound to Page's upper bound given by eqn. 5.25, upper bound based on the Hilbert space dimension in the virtual legs, and the numerical entropy in equilibrium. First, we observe that Page's upper bound deviates from the numerical result because of the finite size of boson sampling device; the Hilbert space dimension estimation is to further justify that the singular value distribution are flat for all subsystem size; otherwise, the calculation will deviate a lot from the numerical result. Finally, we can see that our estimated upper bound does describe the entanglement entropy with small systematic deviation.

6.4 General Discussion

At this rate, we have studied two types of bosonic circuits: fibre loops set-up and boson sampling devices. Fibre loops are represented in TNS as sequential unitary operations on the input state. Meanwhile, parallel unitary operations for boson sampling devices. In this dissertation are three reasons to pursue the study of bosonic circuits with TNS.

First, as demonstrated throughout the theoretical analysis, we have been utilizing properties of TN to make arguments for the analytic upper bounds of the entanglement entropy, which turn out to be correct.

Secondly, TNS provides, as stated in the introduction, a direct and precise measurement of the simulation hardness of a quantum system. In our case, we have shown that computational time of the fibre loop states scales linearly with the system size simply by proving the area law entanglement entropy; we showed that for both types of circuits the computational time scales polynomially with the number of particles added to the system, simply because the entanglement entropy scales as logarithmic; we also showed that boson sampling device has entanglement entropy that scales linearly with the system size, meaning that these devices are exponentially hard to simulate. From TNS, we can easily classify the scaling of the entropy concerning the architecture and tell us what parameters – photon number in our case – are insensitive to the architecture. Without the guidance of the TNS, the tasks above will be much harder to finish.

Finally, this dissertation also serves as an attempt to simulate photon states beyond the phase space formalism. It is well-known that the phase space formalism is well-suited to describe the Gaussian state of photons, but it is not as efficient in doing so in describing non-Gaussian state[48]. Through the analysis, the TNS demonstrates that it can simulate efficiently the fibre loop set-up for a fixed amount of loops. The whole MPS description of fibre loop set-up is an example of a non-Gaussian state that follows the area law. In this respect, it is more efficient to simulate with TNS than with phase space formalism. The conclusion from the analysis is that TNS is useful for simulating non-Gaussian states that follow the area law entanglement entropy.

Chapter 7

Conclusion

7.1 Summary of Thesis Achievements

In the dissertation, we first review the concept of TN, types of TN, simulation techniques, and the mathematics involved with the MPS – canonical form and TEBD – that is necessary for our analysis. With the canonical form, we describe its power and limitation, although it turns out to be useful to provide information for the entanglement entropy analytic upper bound despite the circumstance. For the TEBD, we explain the Suzuki-Trotter approximation and the algorithm for tensor contraction. Interestingly, the Suzuki-Trotter approximation reappears in our derivation of the analytic upper bound. After the basics, we dig deeper into the charge conservation law with TNS, studying it in terms of the CSC and Wigner-Eckart theorem that is theoretically important for subjects like the spin network and to reduce the memory cost by factoring out the CSC in a TN.

In the second part, we apply the materials to study different types of bosonic circuits. With the help of the TN formalism, we manage to derive the analytic upper bound of fibre loop bosonic circuit, and boson sampling device with parallel cross-Kerr interactions at small parameters τ and λ, and the result agrees with the numerical simulation. Meanwhile, we numerically estimate the universal analytic upper bound for the boson sampling device, which is believed to be correct due to its theoretical background and the simulation result.

Throughout the dissertation, TN state plays a crucial role in deriving the analytic expression and classifying the simulation difficulty of a quantum system based on its entanglement spectrum. TNS expresses entanglement property in such an explicit form that it simplifies a lot of the calculation. To calculate the entanglement spectrum, for example, we just need to read off the singular values of the MPS. The effect of the entropy size has a direct effect on the computational time of the simulation. For example, the reason why the boson sampling simulation is kept at $L = 10$ is that the program computational cost increases drastically when we introduce $L = 12$. Meanwhile, the effect is not as dramatic as we multiply the photon numbers by 2. These causes of these effects are all addressed in the analysis of the MPS entanglement entropy. However, one property that the TNS does not address is the lower bound of the entanglement entropy simply due to the nature of the triangular inequality. For that purpose, TNS alone is not sufficient and that would require extra mathematics.

7.2 Applications

At the very least, we hope that our review can encourage readers to learn TNS. As mentioned in the introduction, the application of TNS is extremely broad – encompassing condensed matter, quantum information, quantum gravity, and neuroscience, and unfortunately, this dissertation reveals only the tip of the iceberg. The review focuses on the essential topics such that readers can appreciate the aesthetic of TNS while learning how to construct them.

The analysis throughout the dissertation is used mainly to gauge quantum supremacy. Measuring quantum supremacy plays a critical role in the NISQ era. It tests the effectiveness of a commercial quantum computer in dealing with optimization problems in different sectors such as finance and quantum chemistry. In this respect, TNS appears to be well suited in the gauging process. As mentioned, there are already researches that utilize TNS to determine the effect of photon loss on quantum complexity. We draw inspirations from these applications and derive and estimate the analytic upper bound for the lossless case. The techniques we used are very useful to classify the complexity of a general quantum circuit with or without loss.

Otherwise, it is still interesting to study the properties of entanglement entropy and its relationship to a one-dimensional geometry.

7.3 Future Work

The first work to continue is to analytically derive the boson sampling analytic upper bound. The derivation is not expected to be extremely difficult, but there are a few technical details to be sorted out before the argument can be made concrete.

As an extension to the current work, we showed numerically that the quantum walk model follows the area law at a high transmission coefficient, but no further work is done in this direction. For low transmission, the particle appears to be instead stationary with the wave packet spreads out over time. This direction is extremely interesting to pursue. It to some extent reveals the relationship between entanglement entropy and casual set structure. For our example, a high transmission coefficient corresponds to a particle that travels at nearly the speed of light in the causal set of beam-splitter. Then, the uniform entanglement entropy corresponds to the fact that two entangled photons traveling to the opposite directions always have a fixed entanglement entropy despite the distance apart.

Appendix A

Appendix

A.1 Existence of the Canonical Form

Here we will derive the canonical form for the closed boundary condition, and the derivation will also serve as an example of diagrammatic reasoning. Proof using TNS diagrams saves up lots of symbols that are confusing to read and space-consuming.

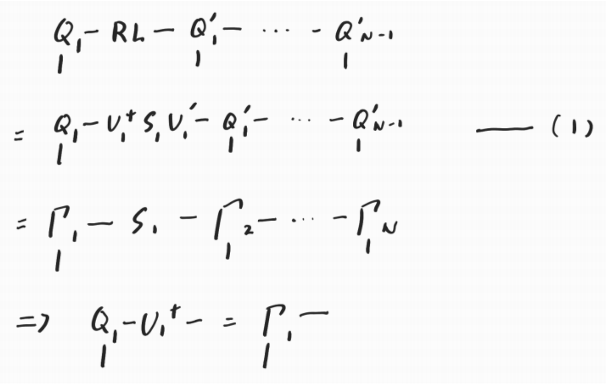
Q₁ − RL − Q′₁ − ⋯ − Q′ₙ₋₁
= Q₁ − U₁⁺ S₁ U₁′ − Q′₁ − ⋯ − Q′ₙ₋₁ —— (1)
= Γ₁ − S₁ − Γ₂ − ⋯ − Γₙ
=> Q₁ − U₁⁺ − = Γ₁ −

Figure A.1: First, we Schmidt decompose the first bond using the QR and LQ decomposition as shown in fig. A.1. Comparing (1) to the full canonical form we find out the form of the boundary Γ_1 tensor, which satisfies eqn. 3.5, because $U_1^\dagger$ is unitary.

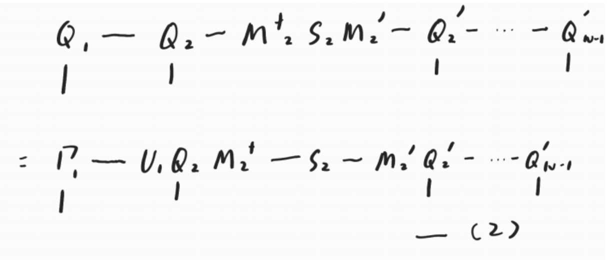

Q_1 — Q_2 — $M_2^\dagger S_2 M_2'$ — Q_2' — ⋯ — Q_{N-1}'
= Γ_1 — $U_1 Q_2 M_2^\dagger$ — S_2 — $M_2' Q_2'$ — ⋯ — Q_{N-1}'
— (2)

Figure A.2: You need better explanation here. We proceed to Schmidt decompose the second bond.

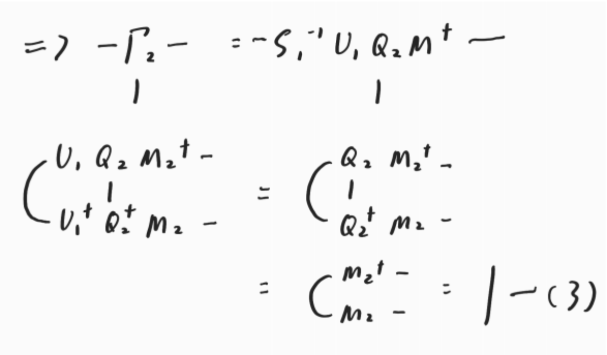

=> $-\Gamma_2-$ = $-S_1^{-1} U_1 Q_2 M^\dagger$ —
$U_1 Q_2 M_2^\dagger$
$U_1^\dagger Q_2^\dagger M_2$
= $Q_2 M_2^\dagger$
$Q_2^\dagger M_2$
= $M_2^\dagger$
M_2
= — (3)

Figure A.3: Comparing (2) with the canonical form, we obtain form of the bulk Γ_2 tensor. We can explicitly check that $S_1\Gamma_2$ satisfies eqn. 3.13.

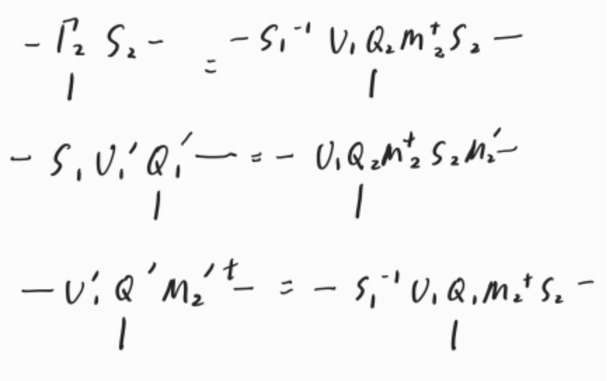

$-\Gamma_2 S_2-$ = $-S_1^{-1} U_1 Q_2 M_2^\dagger S_2$ —
$-S_1 U_1' Q_1'$ — = — $U_1 Q_2 M_2^\dagger S_2 M_2'$ —
$-U_1' Q' M_2'^\dagger$ — = — $S_1^{-1} U_1 Q_1 M_2^\dagger S_2$ —

Figure A.4: Meanwhile, we demand that $\Gamma_2 S_2$ needs to satisfy eqn. 3.14. Comparing (1) and (2), we can simply the equation $\Gamma_2 S_2 = S_1^{-1} U_1 Q_2 M_2^\dagger S_2$.

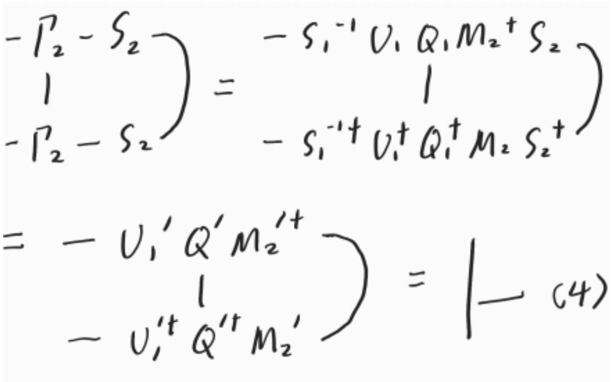

$-\Gamma_2 - S_2$
$-\Gamma_2 - S_2$
= — $S_1^{-1} U_1 Q_1 M_2^\dagger S_2$
— $S_1^{-1\dagger} U_1^\dagger Q_1^\dagger M_2 S_2^\dagger$
= — $U_1' Q' M_2'^\dagger$
— $U_1'^\dagger Q'^\dagger M_2'$
= — (4)

Figure A.5: Thus, we also verify eqn. 3.14. The rest of the tensor Γ_i can be constructed via the same method, and they must all satisfy (3) and (4) by construction.

A.2 TEBD Preserves Canonical Form

Up next we prove that TEBD does not affect the canonical form.

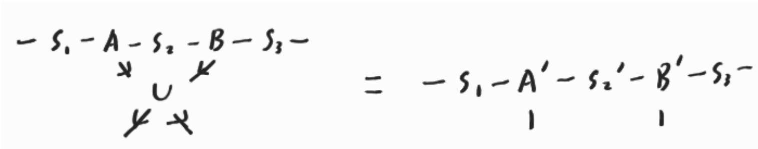
s₁ A s₂ B s₃
U
=
s₁ A' s₂' B' s₃

Figure A.6: Consider two lattice sites A and B of the canonical form with three singular values s_1, s_2 and s_3. We operate U obtained from Suzuki-Trotter decomposition on the physical legs and SVD to obtain the new "canonical form". By definition of SVD, s_2A' and $B's_3$ are guaranteed to be isometric, but we want to show that $A's_2'$ and $s_2'B'$ are also isometric.

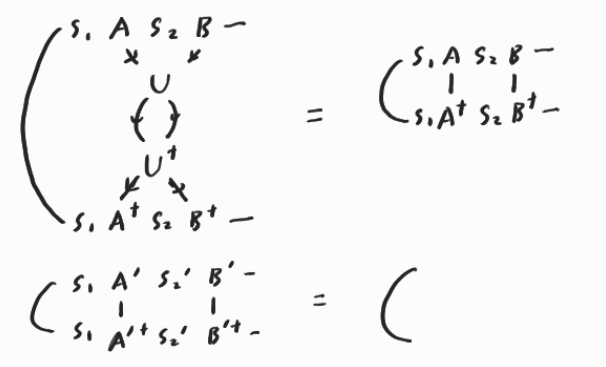
s₁ A s₂ B
U
U†
s₁ A† s₂ B†
=
s₁ A s₂ B
s₁ A† s₂ B†
s₁ A' s₂' B'
s₁ A'† s₂' B'†
=

Figure A.7: By unitarity, we observe that $s_1A's_2'B'$ must be isometric simply because s_1As_2B is isometric.

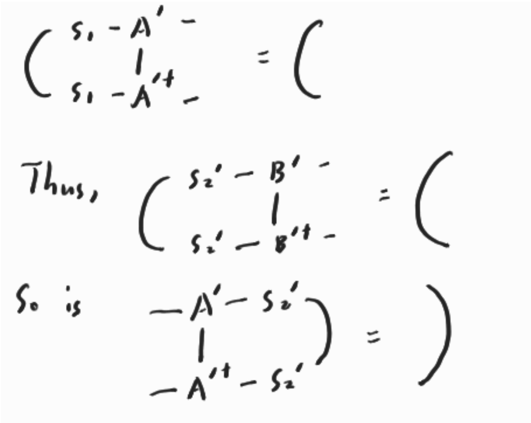
s₁ A'
s₁ A'†
=
Thus,
s₂' B'
s₂' B'†
=
So is
A' s₂'
A'† s₂'
=

Figure A.8: Meanwhile, as mentioned in the beginning, s_1A' is also isometric due to property of SVD, so $s_2'B'$ is also isometric. With the same reasoning, it is also true for $A's_2'$. Thus, the new MPS is in canonical form!

A.3 Two fibre loops Canonical Form

Here we show that the two fibre loops architectures are in their natural right canonical form.

We consider the two types of two loops architecture tensor network:

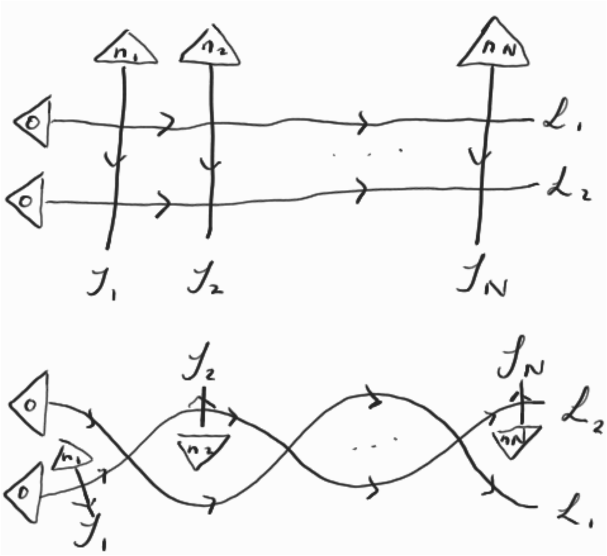
n_1
n_2
n_N
0
$\mathcal{L}_1$
0
$\mathcal{L}_2$
$\mathcal{J}_1$
$\mathcal{J}_2$
$\mathcal{J}_N$
$\mathcal{J}_2$
$\mathcal{J}_N$
0
$\mathcal{L}_2$
n_1
n_2
n_N
0
$\mathcal{J}_1$
$\mathcal{L}_1$

Figure A.9: TNS representations of two loops architecture: the top TNS represents the TNS for the loops in sequence architecture, and the bottom one represents the TNS for the loop in loop architecture. The intersection is where the unitary operator locates and the time direction specifies by the arrow, is how to identify the unitarity.

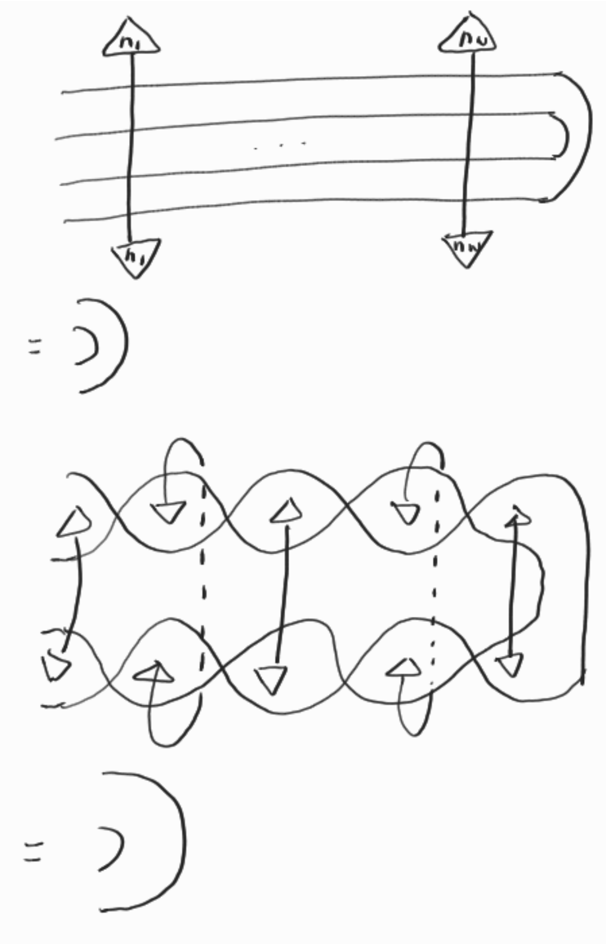

Figure A.10: By the property of unitarity, the right side of the MPS can be reduced to the Kronecker delta simply due to unitarity, and that implies that the right side of the two loops architecture is always isometric, thus does not contribute to the entanglement.

Bibliography

[1] J. Preskill, "Quantum computing in the nisq era and beyond," *Quantum*, vol. 2, p. 79, Aug 2018.

[2] R. García-Patrón, J. J. Renema, and V. Shchesnovich, "Simulating boson sampling in lossy architectures," *Quantum*, vol. 3, p. 169, Aug 2019.

[3] G. Evenbly and G. Vidal, "Tensor network states and geometry," *Journal of Statistical Physics*, vol. 145, p. 891–918, Jun 2011.

[4] B. Coecke, "Quantum picturalism," *Contemporary Physics*, vol. 51, p. 59–83, Jan 2010.

[5] Y. O. Nakagawa, M. Watanabe, H. Fujita, and S. Sugiura, "Universality in volume-law entanglement of scrambled pure quantum states," *Nature Communication*, vol. 9, no. 1635, 2018.

[6] R. Penrose, *Tensor methods in algebraic geometry.* PhD thesis, St. John's College, University of Cambridge, 1957.

[7] J.-H. Kim, M. S. H. Oh, and K.-Y. Kim, "Boosting vector calculus with the graphical notation," 2020.

[8] R. S. André Joyal, "Bit-vector algorithms for binary constraint satisfaction and subgraph isomorphism," *Advances in Mathematics*, vol. 88, pp. 55–112, 1991.

[9] J. van de Wetering, "Zx-calculus for the working quantum computer scientist," 2020.

[10] A. Pellionisz and R. Llinás, "Tensorial approach to the geometry of brain function: Cerebellar coordination via a metric tensor," *Neuroscience*, vol. 5, no. 7, pp. 1125–1136, 1980.

[11] R. Orús, "A practical introduction to tensor networks: Matrix product states and projected entangled pair states," *Annals of Physics*, vol. 349, p. 117–158, Oct 2014.

[12] A. J. Ferris, "Unbiased monte carlo for the age of tensor networks," 2015.

[13] S. Paeckel, T. Köhler, A. Swoboda, S. R. Manmana, U. Schollwöck, and C. Hubig, "Time-evolution methods for matrix-product states," *Annals of Physics*, vol. 411, p. 167998, Dec 2019.

[14] U. Schollwöck, "The density-matrix renormalization group," *Rev. Mod. Phys.*, vol. 77, pp. 259–315, Apr 2005.

[15] J. Eisert, M. Cramer, and M. B. Plenio, "Colloquium: Area laws for the entanglement entropy," *Reviews of Modern Physics*, vol. 82, p. 277–306, Feb 2010.

[16] N. Bao, C. Cao, S. M. Carroll, A. Chatwin-Davies, N. Hunter-Jones, J. Pollack, and G. N. Remmen, "Consistency conditions for an ads multiscale entanglement renormalization ansatz correspondence," *Physical Review D*, vol. 91, Jun 2015.

[17] S. Singh and G. Vidal, "Tensor network states and algorithms in the presence of a global su(2) symmetry," *Physical Review B*, vol. 86, Nov 2012.

[18] M. Han and L.-Y. Hung, "Loop quantum gravity, exact holographic mapping, and holographic entanglement entropy," *Physical Review D*, vol. 95, Jan 2017.

[19] M. Lubasch, J. I. Cirac, and M.-C. Bañuls, "Algorithms for finite projected entangled pair states," *Phys. Rev. B*, vol. 90, p. 064425, Aug 2014.

[20] G. Evenbly and G. Vidal, "Algorithms for entanglement renormalization," *Physical Review B*, vol. 79, Apr 2009.

[21] A. Pathak, *Elements of Quantum Computation and Quantum Communication.* USA: Taylor Francis, Inc., 1st ed., 2013.

[22] U. Schollwöck, "The density-matrix renormalization group in the age of matrix product states," *Annals of Physics*, vol. 326, p. 96–192, Jan 2011.

[23] G. Vidal, "Efficient simulation of one-dimensional quantum many-body systems," *Phys. Rev. Lett.*, vol. 93, p. 040502, Jul 2004.

[24] J. M. Hauschild, *Quantum Many-Body Systems Far Out of Equilibrium — Simulations with Tensor Networks.* PhD thesis, Technical University of Munich, 2019.

[25] M. Vekić and S. R. White, "Smooth boundary conditions for quantum lattice systems," *Phys. Rev. Lett.*, vol. 71, pp. 4283–4286, Dec 1993.

[26] L. Cincio and G. Vidal, "Characterizing topological order by studying the ground states on an infinite cylinder," *Phys. Rev. Lett.*, vol. 110, p. 067208, Feb 2013.

[27] M. Suzuki, "Generalized trotter's formula and systematic approximants of exponential operators and inner derivations with applications to many-body problems," *Communications in Mathematical Physics*, vol. 51, p. 183–190, 1976.

[28] C. Guo and D. Poletti, "Matrix product states with adaptive global symmetries," *Physical Review B*, vol. 100, Oct 2019.

[29] S. Singh, R. N. C. Pfeifer, and G. Vidal, "Tensor network states and algorithms in the presence of a global u(1) symmetry," *Physical Review B*, vol. 83, Mar 2011.

[30] S. Singh, "Tensor network states and algorithms in the presence of abelian and non-abelian symmetries," 2012.

[31] A. Weichselbaum, "Non-abelian symmetries in tensor networks: A quantum symmetry space approach," *Annals of Physics*, vol. 327, p. 2972–3047, Dec 2012.

[32] J. H. William Fulton, *Representation Theory: a First Course.* Berlin: Springer, 1991.

[33] T. Soejima, K. Siva, N. Bultinck, S. Chatterjee, F. Pollmann, and M. P. Zaletel, "Isometric tensor network representation of string-net liquids," *Physical Review B*, vol. 101, Feb 2020.

[34] T. Lan and X.-G. Wen, "Topological quasiparticles and the holographic bulk-edge relation in(2+1)-dimensional string-net models," *Physical Review B*, vol. 90, Sep 2014.

[35] G. Chirco, D. Oriti, and M. Zhang, “Group field theory and tensor networks: towards a ryu–takayanagi formula in full quantum gravity,” *Classical and Quantum Gravity*, vol. 35, p. 115011, may 2018.

[36] E. Wigner, “On the quantum correction for thermodynamic equilibrium,” *Phys. Rev.*, vol. 40, pp. 749–759, Jun 1932.

[37] M. Lubasch, A. A. Valido, J. J. Renema, W. S. Kolthammer, D. Jaksch, M. S. Kim, I. Walmsley, and R. García-Patrón, “Tensor network states in time-bin quantum optics,” *Physical Review A*, vol. 97, Jun 2018.

[38] C. Oh, K. Noh, B. Fefferman, and L. Jiang, “Classical simulation of lossy boson sampling using matrix product operators,” *Physical Review A*, vol. 104, Aug 2021.

[39] H.-L. Huang, W.-S. Bao, and C. Guo, “Simulating the dynamics of single photons in boson sampling devices with matrix product states,” *Physical Review A*, vol. 100, Sep 2019.

[40] R. A. Campos, B. E. A. Saleh, and M. C. Teich, “Quantum-mechanical lossless beam splitter: Su(2) symmetry and photon statistics,” *Phys. Rev. A*, vol. 40, pp. 1371–1384, Aug 1989.

[41] G. W. Wolfgang Tittel, “Photonic entanglement for fundamental tests and quantum communication,” *Quantum Information and Computation*, vol. 1, no. 2, 2001.

[42] J. J. Sakurai and J. Napolitano, *Modern Quantum Mechanics*. Cambridge University Press, 1985.

[43] G. Evenbly and G. Vidal, “Scaling of entanglement entropy in the (branching) multiscale entanglement renormalization ansatz,” *Physical Review B*, vol. 89, Jun 2014.

[44] D. N. Page, “Average entropy of a subsystem,” *Phys. Rev. Lett.*, vol. 71, pp. 1291–1294, Aug 1993.

[45] M. Headrick, V. E. Hubeny, A. Lawrence, and M. Rangamani, “Causality holographic entanglement entropy,” *Journal of High Energy Physics*, vol. 2014, Dec 2014.

[46] L. Vidmar, L. Hackl, E. Bianchi, and M. Rigol, “Entanglement entropy of eigenstates of quadratic fermionic hamiltonians,” *Physical Review Letters*, vol. 119, Jul 2017.

[47] L. Vidmar and M. Rigol, “Entanglement entropy of eigenstates of quantum chaotic hamiltonians,” *Physical Review Letters*, vol. 119, Nov 2017.

[48] M. Walschaers, “Non-gaussian quantum states and where to find them,” 2021.